





Review

Functionalized Lanthanide Oxide Nanoparticles for Tumor Targeting, Medical Imaging, and Therapy

Mohammad Yaseen Ahmad ¹, Huan Yue ¹, Tirusew Tegafaw ¹, Shuwen Liu ¹, Son Long Ho ¹, Gang Ho Lee ^{1,*},
Sung-Wook Nam ² and Yongmin Chang ^{2,*}

¹ Department of Chemistry, College of Natural Sciences, Kyungpook National University, Taegu 41566, Korea; yaseen.knu@gmail.com (M.Y.A.); yuehuan888@gmail.com (H.Y.); tirukorea@gmail.com (T.T.); liushuwen0701@gmail.com (S.L.); sonlongh@gmail.com (S.L.H.)

² Department of Molecular Medicine, School of Medicine, Kyungpook National University, Taegu 41405, Korea; nams@knu.ac.kr

* Correspondence: ghlee@mail.knu.ac.kr (G.H.L.); ychang@knu.ac.kr (Y.C.)

Abstract: Recent progress in functionalized lanthanide oxide (Ln₂O₃) nanoparticles for tumor targeting, medical imaging, and therapy is reviewed. Among the medical imaging techniques, magnetic resonance imaging (MRI) is an important noninvasive imaging tool for tumor diagnosis due to its high spatial resolution and excellent imaging contrast, especially when contrast agents are used. However, commercially available low-molecular-weight MRI contrast agents exhibit several shortcomings, such as nonspecificity for the tissue of interest and rapid excretion in vivo. Recently, nanoparticle-based MRI contrast agents have become a hot research topic in biomedical imaging due to their high performance, easy surface functionalization, and low toxicity. Among them, functionalized Ln₂O₃ nanoparticles are applicable as MRI contrast agents for tumor-targeting and nontumor-targeting imaging and image-guided tumor therapy. Primarily, Gd₂O₃ nanoparticles have been intensively investigated as tumor-targeting T₁ MRI contrast agents. T₂ MRI is also possible due to the appreciable paramagnetic moments of Ln₂O₃ nanoparticles (Ln = Dy, Ho, and Tb) at room temperature arising from the nonzero orbital motion of 4f electrons. In addition, Ln₂O₃ nanoparticles are eligible as X-ray computed tomography contrast agents because of their high X-ray attenuation power. Since nanoparticle toxicity is of great concern, recent toxicity studies on Ln₂O₃ nanoparticles are also discussed.

Keywords: imaging agent; lanthanide oxide nanoparticle; tumor targeting; toxicity



Citation: Ahmad, M.Y.; Yue, H.; Tegafaw, T.; Liu, S.; Ho, S.L.; Lee, G.H.; Nam, S.-W.; Chang, Y. Functionalized Lanthanide Oxide Nanoparticles for Tumor Targeting, Medical Imaging, and Therapy. *Pharmaceutics* **2021**, *13*, 1890. <https://doi.org/10.3390/pharmaceutics13111890>

Academic Editor: Igor Chourpa

Received: 30 September 2021

Accepted: 5 November 2021

Published: 8 November 2021

Publisher's Note: MDPI stays neutral with regard to jurisdictional claims in published maps and institutional affiliations.



Copyright: © 2021 by the authors. Licensee MDPI, Basel, Switzerland. This article is an open access article distributed under the terms and conditions of the Creative Commons Attribution (CC BY) license (<https://creativecommons.org/licenses/by/4.0/>).

1. Introduction

Medical imaging plays an important role in the pre-detection, diagnosis, and treatment of tumors [1]. Among the currently available medical imaging techniques, magnetic resonance imaging (MRI) allows whole-body imaging and outstanding microsoft tissue contrast and image resolution to reveal morphological and anatomical details of tissues [2,3]. As imaging agents, various nanoparticles have been developed due to their remarkable physical and chemical properties, which are superior to those of small molecules [4–7]. Moreover, nanoparticles can be easily surface-functionalized for advanced imaging and tumor targeting [8,9]. They can also provide longer blood circulation times than small molecules, which is conducive to tumor targeting and drug delivery to specific tumor cells [10,11].

Lanthanide oxide (Ln₂O₃) nanoparticles (Ln = Gd, Tb, Dy, and Ho) are of special interest because they have appreciable magnetic moments at room temperature, which is useful for MRI [12–15], and high X-ray attenuation power, which is useful for X-ray computed tomography (CT) [16–18]. In addition, surface-modified Ln₂O₃ nanoparticles exhibit improved properties, such as high-water proton spin relaxivities, high colloidal stabilities, and low toxicities [12–14]. For in vivo applications, nanoparticles should have an ultrasmall particle diameter (<3 nm) to allow their excretion from the body via the urinary system after

intravenous injection [19,20]. Ln_2O_3 nanoparticles meet such requirements, displaying excellent MRI and CT imaging properties at ultrasmall particle diameters [12–15].

The development of tumor-targeting Ln_2O_3 nanoparticles is challenging. Especially when compared with commercial molecular Gd-chelates [21–23], Gd_2O_3 nanoparticles are more efficient longitudinal relaxation promoters [12–15] because their longitudinal relaxation (r_1) values are higher than those (i.e., $3\text{--}5\text{ s}^{-1}\text{mM}^{-1}$) [21–23] of commercial molecular MRI contrast agents. Therefore, Gd_2O_3 nanoparticles can provide very high contrast T_1 MR images and thus, are ideal candidates for tumor-targeting T_1 MRI contrast agents. In particular, their r_1 value is optimal at ultrasmall nanoparticle size (1.0–2.5 nm) [24,25]. Meanwhile, other Ln_2O_3 nanoparticles ($\text{Ln} = \text{Dy}, \text{Tb}, \text{and Ho}$) are eligible as T_2 MRI contrast agents [12,13,15].

Nanoparticles alone accumulate nonspecifically in tumors via passive targeting, i.e., the enhanced permeability and retention (EPR) effect [26]. The accumulation amount and specificity to tumors can be enhanced by active targeting, which is commonly achieved by modifying contrast agents with tumor-targeting ligands that can selectively bind to receptors overexpressed on tumor-cell membranes. Such tumor-targeting ligands include small molecules, such as arginylglycylaspartic acids (Arg-Gly-Asp or RGDs) [27–29] and folic acid [30,31], peptides, such as chlorotoxin (CTX) [32,33], and biological molecules, such as antibodies [34]. Nanoparticles can provide a flexible platform to attach tumor-targeting ligands, thereby improving their specificity and effectiveness for tumor treatment. In addition, anticancer drugs can also be attached to nanoparticle surfaces for chemotherapy. Generally, in this type of treatment, most anticancer drugs cannot differentiate between tumor and normal cells, causing toxic side effects [35,36]. However, such side effects can be minimized or eliminated by delivering drugs via tumor-targeting nanoparticles. However, the cytotoxicity and biocompatibility of lanthanides during and after endocytosis by cells are still largely unknown, although numerous reports describe lanthanides as relatively non-toxic elements [37,38].

The main purpose of this review is to provide an insight into tumor imaging and image-guided tumor therapy using functionalized (i.e., tumor-targeting ligand-conjugated) Ln_2O_3 nanoparticles. First, nanoparticle synthesis methods, surface-modification, tumor-targeting ligand conjugation, and various experimental analyses for Ln_2O_3 nanoparticles are introduced. Second, physicochemical properties, such as particle diameters and magnetic properties, and imaging properties, including relaxivities, are discussed. Third, recent developments of tumor-targeting T_1 MRI contrast agents based on Gd_2O_3 nanoparticles that were applied in tumor imaging and image-guided tumor therapy and Ln_2O_3 nanoparticle-based T_2 MRI and CT contrast agents are discussed. Finally, recent progress in the knowledge of the toxicity of Ln_2O_3 nanoparticles is discussed. Overall, this review provides an overview of the recent progress in functionalized Ln_2O_3 nanoparticles applied in tumor imaging and therapy.

2. Synthesis and Surface Functionalization of Ln_2O_3 Nanoparticles

Among the various methods currently available for the synthesis of ultrasmall Ln_2O_3 nanoparticles, the synthesis in a polyol solvent is preferred for biomedical applications because ultrasmall nanoparticles are obtained (average particle diameter = 2.0 nm) and subsequent surface coating of the nanoparticles with hydrophilic and biocompatible ligands can be performed in one pot [17,31]. A general reaction scheme for the polyol synthesis is provided in Figure 1.

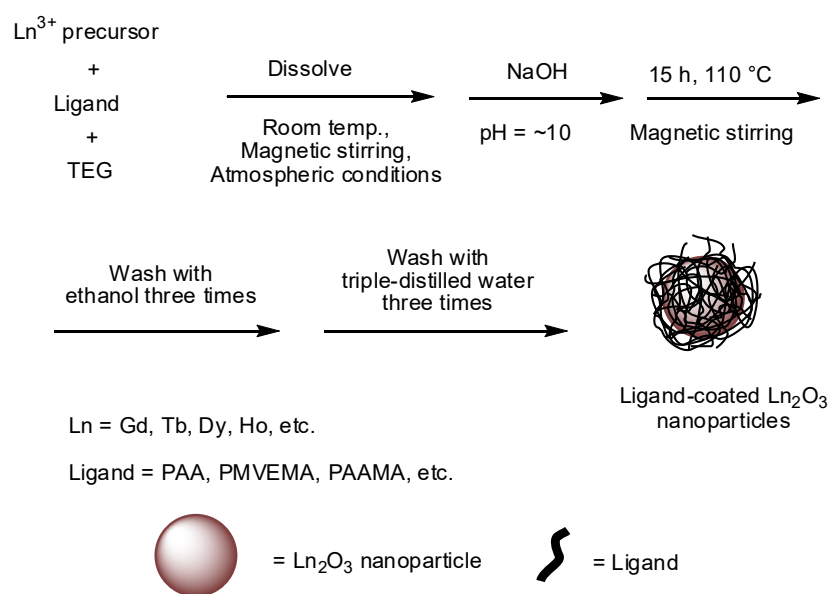


Figure 1. Reaction scheme for the one-pot polyol synthesis of hydrophilic and biocompatible polymer-coated ultrasmall Ln_2O_3 nanoparticles. TEG = triethylene glycol.

Nanoparticle contrast agents possess an additional advantage over molecular agents because cancer-targeting ligands and drugs can be easily attached to the nanoparticle surfaces. Small molecular ligands are less efficient in providing good colloidal stability to nanoparticles compared with polymer ligands, which is due to the presence of many hydrophilic binding groups in the polymers for attachment to the nanoparticles [39–43]. In addition, hydrophilic polymers can provide higher r_1 values than small molecular ligands [39–41] because they can attract more water molecules around the nanoparticles. Examples of these polymers are polyacrylic acid (PAA), polymethyl vinyl ether-alt-maleic acid (PMVEMA), and polyacrylic acid-co-maleic acid (PAAMA) having numerous COOH groups (Figure 1) [39–41], which can serve as anchor groups of functional molecules, such as cancer-targeting ligands and drugs. For example, RGD-conjugated PAA-coated Gd_2O_3 nanoparticles were reported by Ho et al. [44] (Figure 2).

Ln_2O_3 nanoparticles can also be synthesized in organic solvents via the thermal decomposition method. The synthesized nanoparticles can be further coated with hydrophilic ligands and then conjugated with cancer-targeting ligands. For example, CTX-poly(ethylene glycol)-*N*-(trimethoxysilylpropyl) ethylenediamine triacetic acid silane-coated Gd_2O_3 nanoparticles (CTX-PEG-TETT- Gd_2O_3) were reported by Gu et al. [45] as tumor-targeting contrast agents (Figure 3). Here, the biocompatible poly(ethylene glycol) (PEG) layer is known to stabilize the Gd_2O_3 nanoparticles, enhance blood circulation blood times, and improve colloidal stability [11].

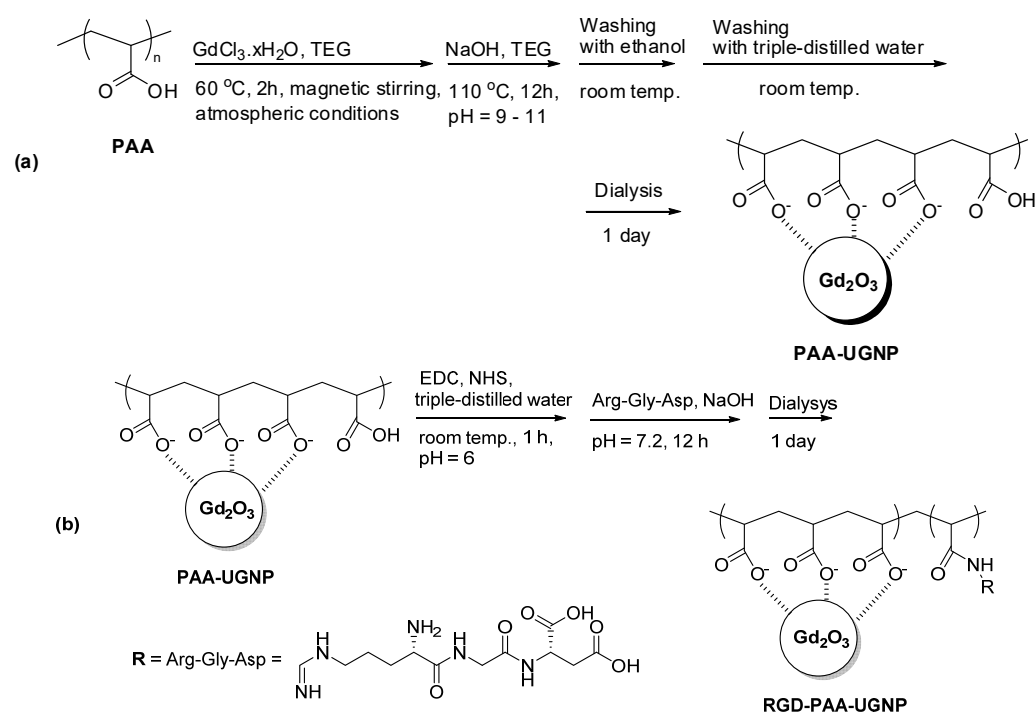


Figure 2. Two-step synthesis of RGD-PAA-Gd₂O₃ nanoparticles. (a) Step 1: PAA-Gd₂O₃ nanoparticles and (b) step 2: conjugation of RGD with PAA-Gd₂O₃ nanoparticles. EDC = *N*-(3-dimethylaminopropyl)-*N'*-ethylcarbodiimide, NHS = *N*-hydroxysuccinimide, and UGNP = ultrasmall gadolinium oxide nanoparticle. Adapted with permission from [44], The Royal Society of Chemistry, 2020.

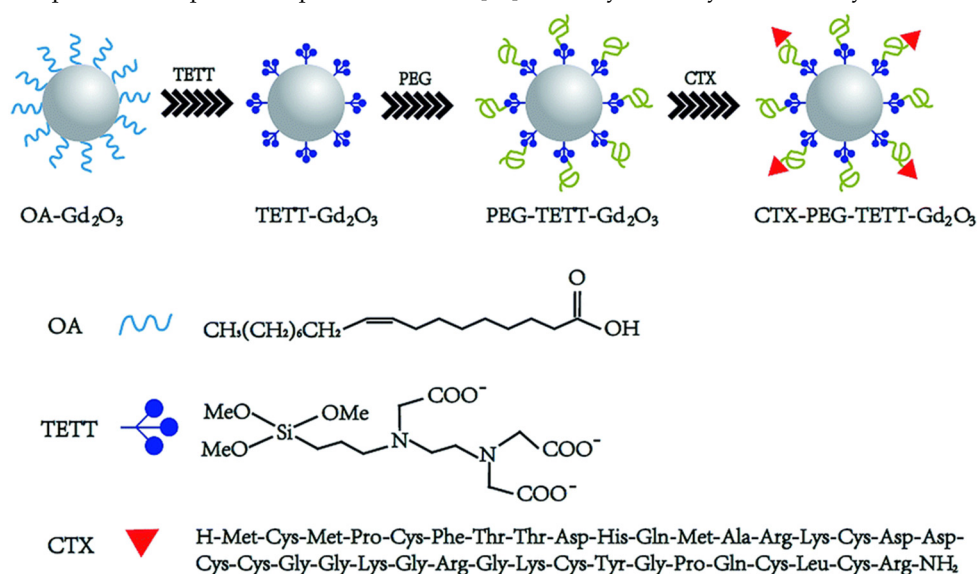


Figure 3. Schematic illustration for the synthesis of CTX-PEG-TETT-Gd₂O₃ nanoparticles. TETT = *N*-(trimethoxysilylpropyl) ethylenediamine triacetic acid trisodium salt and OA = oleic acid. Reproduced from [45], The Royal Society of Chemistry, 2014.

3. Physicochemical Characterization

Various experimental techniques can be used to characterize the synthesized Ln₂O₃ nanoparticles [17,31], as summarized in Table 1. The particle diameters, the hydrodynamic diameters of nanoparticles dispersed in water, and the crystal structure of the nanoparticles can be measured using a high-resolution transmission electron microscope (HRTEM) operating at high acceleration voltages (>200 kV), a dynamic light scattering (DLS) particle size analyzer, and a powder X-ray diffraction (XRD) spectrometer, respectively. The

attachment of ligands on the nanoparticle surfaces can be investigated by recording Fourier transform-infrared (FT-IR) absorption spectra using powder samples; powder samples may be pelletized in KBr for easy handling and acquisition of good signal-to-noise ratios using a small number of powder samples. The amount of surface-coating ligand can be estimated according to thermogravimetric analysis (TGA) curves. The elemental analysis (EA) can also be used to investigate the surface-coating amount and ligand composition (C/H/O/N/S) in metal oxide nanoparticles because metal oxide nanoparticles hardly decompose during EA. The Ln-concentration in an aqueous nanoparticle suspension can be determined using an inductively coupled plasma atomic emission spectrometer (ICPAES). The *in vitro* cellular cytotoxicity of the ligand-coated Ln_2O_3 nanoparticles can be measured using various cell viability assay techniques, such as trypan blue dye exclusion staining, methylthiazoly tetrazolium (MTT) reduction, and water-soluble tetrazolium salt (WST) assay [46]. Cell viability measurements are generally performed using more than two cell lines to obtain consistent and reliable results because the cell viabilities generally depend on the cell lines. Magnetization (M) values of the nanoparticles can be estimated by recording M versus applied field (H) (M–H) curves at room temperature using a vibrating sample magnetometer (VSM). Net M values of the nanoparticles without ligand can be obtained using the net mass of the nanoparticles determined via TGA. For MRI contrast agents, r_1 and the transverse relaxivity (r_2) represent their ability to act as T_1 or T_2 MRI contrast agents. To measure the r_1 and r_2 values, longitudinal (T_1) and transverse (T_2) relaxation times are measured using an MRI scanner. The T_1 relaxation time measurements can be conducted using an inversion recovery method. For the T_2 relaxation times, the Carr–Purcell Meiboom–Gill pulse sequence can be used for multiple spin-echo measurements. The r_1 and r_2 values are then estimated from the slopes of the plots of $1/T_1$ and $1/T_2$ versus the Ln-concentration, respectively. *In vivo* T_1 or T_2 MR images can be obtained using an MRI scanner after intravenous injection of an aqueous nanoparticle suspension sample. In addition, the X-ray attenuation power of Ln_2O_3 nanoparticles, which is higher than those of commercial iodine CT contrast agents, can be measured by recording phantom images using a CT scanner, and *in vivo* CT images can be obtained using a CT scanner after intravenous injection of an aqueous nanoparticle suspension sample.

Table 1. Summary of physicochemical characterization.

| Properties | Technique ¹ | Properties | Technique ¹ |
|--------------------------------|------------------------|------------------------------|------------------------|
| Particle diameter | HRTEM | Hydrodynamic diameter | DLS |
| Crystal structure | XRD | Ligand surface coating | FT-IR absorption, EA |
| Ligand surface-coating amount | TGA, EA | Metal concentration in water | ICPAES |
| Cellular cytotoxicity | MTT, WST | Magnetization | VSM |
| Relaxivity (r_1 and r_2) | MRI | MR image | MRI |
| X-ray attenuation power | CT | CT image | CT |

¹ HRTEM = high-resolution transmission electron microscope; DLS = dynamic light scattering; XRD = X-ray diffraction; FT-IR = Fourier transform-infrared; EA = elemental analysis; TGA = thermogravimetric analysis; ICPAES = inductively coupled plasma atomic emission spectrometry; MTT = methylthiazoly tetrazolium; WST = water-soluble tetrazolium salt; VSM = vibrating sample magnetometer; MRI = magnetic resonance imaging; CT = computed tomography.

4. Physicochemical and Imaging Properties

4.1. Particle Diameters and Surface Coatings

The imaging properties of nanoparticles depend on their particle and hydrodynamic diameters. Ln_2O_3 nanoparticles synthesized via the polyol method generally have ultra-small diameters (average particle diameter = 2.0 nm) [39–44]. Figure 4a–c shows various HRTEM images of Gd_2O_3 nanoparticles [44,47,48]. Both particle and hydrodynamic diameters follow a log-normal function distribution; therefore, average particle and hydrodynamic diameters can be obtained by fitting the log-normal distribution function to the observed particle and hydrodynamic diameter distributions, respectively. The insets in Figure 4c show a nanoparticle suspension sample exhibiting laser light scattering (i.e., Tyndall effect) due to the collision of the nanoparticle colloids with the passing laser light,

whereas triple-distilled water shows no light scattering [44]. This experiment shows the good colloidal dispersion of the nanoparticles in aqueous media.

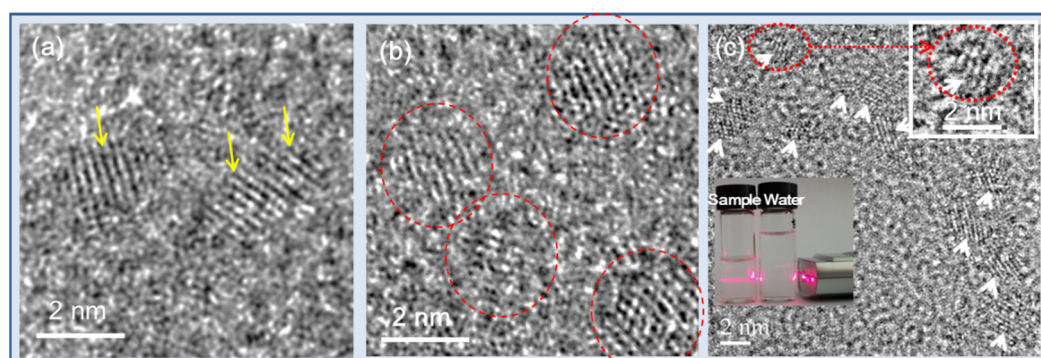


Figure 4. (a–c) HRTEM images [44,47,48]. Arrows and circles indicate nanoparticles. Insets in (c) show a magnified image of a nanoparticle (top right) and laser light scattering (i.e., Tyndall effect) due to the collision of the nanoparticle colloids with a passing laser light, whereas triple-distilled water shows no light scattering, confirming the good colloidal dispersion of nanoparticles in aqueous media (bottom left). Reproduced from [44,47,48]. Copyright 2020 The Royal Society of Chemistry [44]; Copyrights 2018 Wiley [47,48].

Due to the ultrasmall particle diameters, the XRD patterns of nanoparticle powder samples are generally broad and amorphous [49,50]. Nevertheless, upon performing a TGA from room temperature to high temperatures (>500 °C), sharp peaks corresponding to the (222), (400), (440), and (622) planes of a highly crystallized form of Ln_2O_3 having cubic structure are observed [50]. Examples of XRD patterns of ligand-coated Gd_2O_3 nanoparticles recorded before (i.e., as-prepared) and after TGA [44,47] are provided in Figure 5. The peak positions and the estimated cell constants of the TGA-analyzed samples are well consistent with those given in the literature [51]. The sharp peaks observed in the XRD patterns after TGA are due to the particle size growth and subsequent crystallization of the nanoparticles (Figure 5a,b), which was confirmed by Kattel et al. on the basis of HRTEM images [50,52].

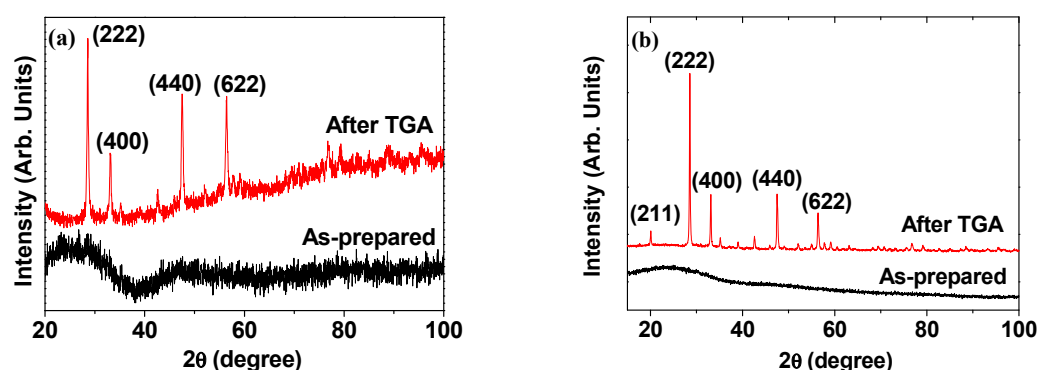


Figure 5. XRD patterns of (a) cRGD- Gd_2O_3 nanoparticles [47] and (b) RGD-PAA- Gd_2O_3 nanoparticles [44] before (i.e., as-prepared; bottom figures) and after TGA (top figures). Adapted from [44,47]. Copyright 2020 The Royal Society of Chemistry [44]; Copyright 2018 Wiley [47].

Surface coating of Ln_2O_3 nanoparticles with hydrophilic and biocompatible ligands is essential for their biomedical applications. The surface coating can be investigated by recording FT-IR absorption spectra. An FT-IR absorption spectrum of PAA-coated Gd_2O_3 nanoparticles is provided as an example at the bottom of Figure 6a [39], along with an FT-IR absorption spectrum of PAA ($M_w = 5100$ Da) at the top of the same figure as a reference. The spectrum of the PAA-coated Gd_2O_3 nanoparticles exhibited a series of bands stemming from PAA, such as C–H stretching (2930 cm^{-1}), COO^- antisymmetric

stretching (1550 cm^{-1}), and COO^- symmetric stretching vibrations (1400 cm^{-1}). The PAA and the nanoparticle were bonded through a coordination bonding between Gd^{3+} on the nanoparticle surface as a hard acid and the COO^- group of PAA as a hard base [53–55]. In this case, a stable nanoparticle colloid was formed in aqueous media because of the multiple bonding between many COO^- groups of PAA (each PAA has ~ 54 COO^- groups) and a nanoparticle. On this basis, the bonding between PAA and the Gd_2O_3 nanoparticle surface was proposed, as displayed in Figure 6b. Another example of surface coating on Gd_2O_3 nanoparticles is provided in Figure 6c, which displayed the FT-IR absorption spectra of RGD, PAA ($M_w = 1800$ Da), PAA- Gd_2O_3 , and RGD-PAA- Gd_2O_3 powder samples [44]. The presence of a C=O stretching band (1553 cm^{-1}) of PAA in the FT-IR absorption spectrum of PAA- Gd_2O_3 nanoparticles confirmed the PAA surface coating on the Gd_2O_3 nanoparticles. This band was red-shifted by 144 cm^{-1} compared with free PAA (1697 cm^{-1}), which can be attributed to the coordination bonding between the COO^- groups of PAA and the Gd^{3+} of the Gd_2O_3 nanoparticles. As mentioned above, each PAA can form many coordination bonds with each Gd_2O_3 nanoparticle via a hard acid (Gd^{3+})–hard base (COO^-) interaction [53–55]. The N–H bending vibration at 1544 cm^{-1} and the C–N stretching vibration at 1390 cm^{-1} of RGD [56] appeared in the FT-IR absorption spectrum of the RGD-PAA- Gd_2O_3 nanoparticles, confirming the successful conjugation of RGD to PAA in the PAA- Gd_2O_3 nanoparticles via amide bond formation.

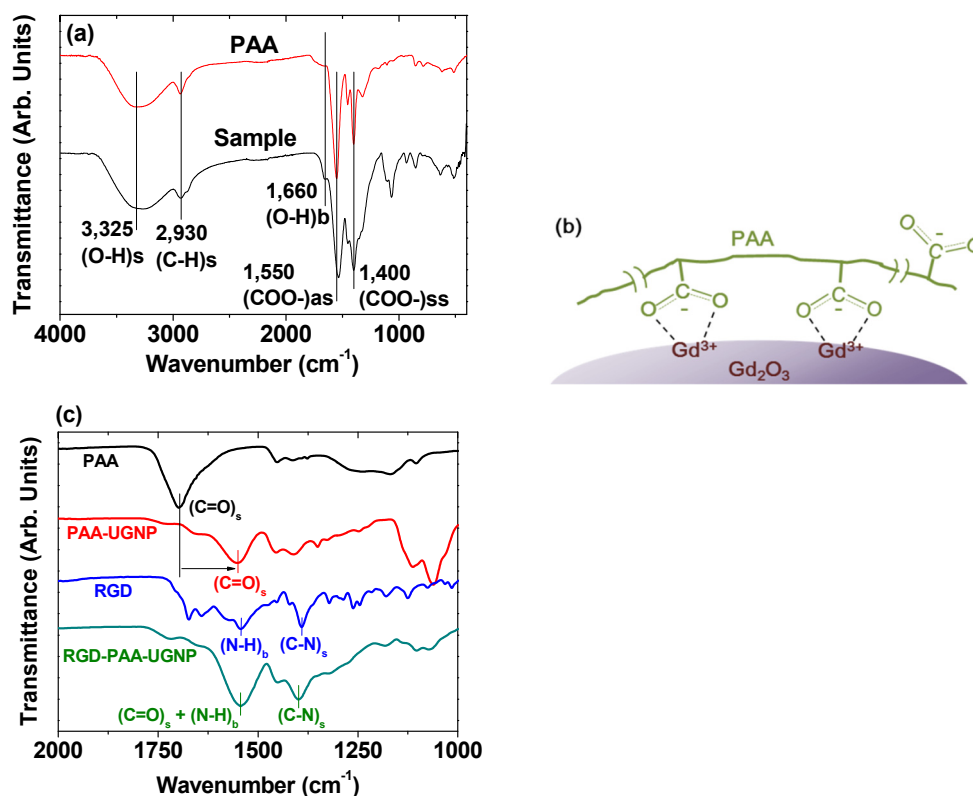


Figure 6. (a) FT-IR absorption spectra of PAA-coated Gd_2O_3 nanoparticles and free PAA sodium salt ($M_w = 5100$ Da) and (b) surface-coating structure of PAA on the Gd_2O_3 nanoparticle surface [39]. (c) FT-IR absorption spectra of PAA ($M_w = 1800$ Da), PAA- Gd_2O_3 nanoparticles, RGD, and RGD-PAA- Gd_2O_3 nanoparticles [44]. The lowercase letters “s”, “ss”, “as”, and “b” indicate stretch, symmetric stretch, antisymmetric stretch, and bend, respectively. Adapted from [39,44]. Copyrights 2018 and 2020 The Royal Society of Chemistry, respectively.

The EA can also be used to investigate the surface coating of nanoparticles. For example, in carbon-coated Gd_2O_3 nanoparticles ($\text{C@Gd}_2\text{O}_3$), the C/H/O content, in which H mostly stems from hydrocarbons and -OH groups and O mostly stems from -OH groups on the carbon-coating layer, was determined to be 28.1/3.2/26.5 in wt% [57]. The sum

of these wt% is 57.8%, which is fairly consistent with the 56.5% estimated from the TGA curve (Figure 7). As can be seen in Figure 7, the remaining 37.0% corresponds to the mass wt% of Gd_2O_3 in the $C@Gd_2O_3$ nanoparticles. By performing a grafting density analysis [58], the wt% can be converted into the number of ligands grafted onto each nanoparticle surface [47,48].

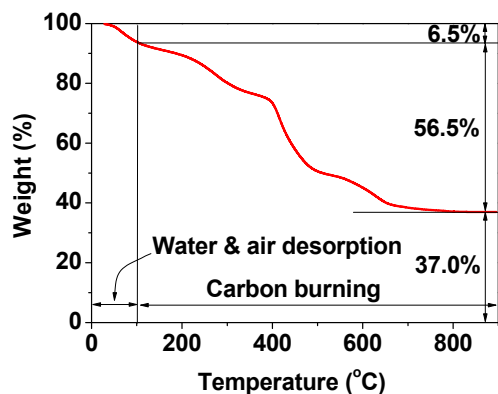


Figure 7. TGA curve of the powder sample of $C@Gd_2O_3$ nanoparticles. Adapted from [57]. Copyright 2019 Elsevier.

4.2. Magnetic Properties

To obtain high r_1 and r_2 values for enhanced MR contrast images, the nanoparticles must exhibit large M values at room temperature [59,60]. Figure 8a,b shows the M – H curves of Ln_2O_3 nanoparticles ($Ln = Gd, Tb, Ho$) [41,43]. Similar to the corresponding bulk materials [61–63], all of the nanoparticle samples are paramagnetic (i.e., no hysteresis, zero coercivity, zero remanence, and low M values) and exhibit appreciable unsaturated M values up to the measured H values at 300 K. From the mass-corrected M – H curve, the net M value of the Gd_2O_3 nanoparticles, which corresponds to the nanoparticles without ligands, at 2.0 T was estimated to be 1.71 emu/g. This appreciable value is due to the high 4f-electron spin magnetic moment ($s = 7/2$) of Gd^{3+} having seven unpaired 4f electrons. Meanwhile, other Ln_2O_3 nanoparticles ($Ln = Tb$ and Ho) exhibit net M values of 3.8 and 4.1 emu/g at 1.8 T (Figure 8b), respectively, which result from high 4f-electron spin–orbital magnetic moments, i.e., $J = 6$ for Tb^{3+} and $J = 8$ for Ho^{3+} . The slightly higher M value of the Ho_2O_3 nanoparticles compared with that of the Tb_2O_3 nanoparticles is due to the higher atomic magnetic moment ($\mu = 10.60 \mu_B$) of Ho^{3+} compared with that of Tb^{3+} ($= 9.72 \mu_B$) [64], where μ_B is the Bohr magneton.

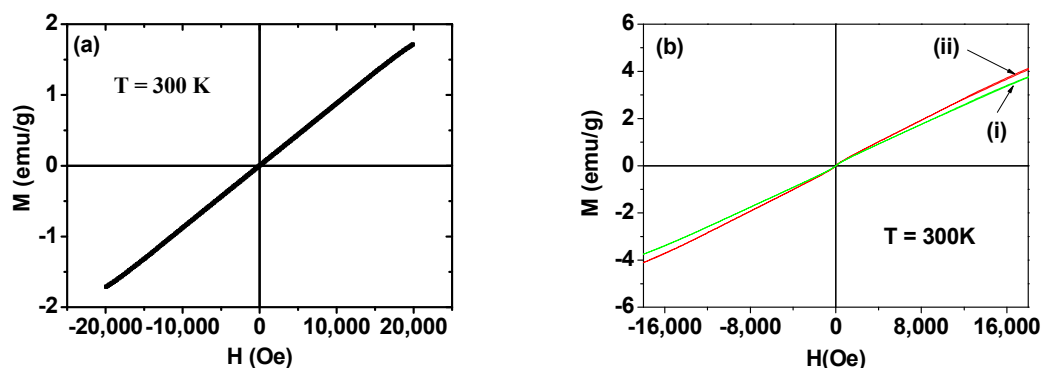


Figure 8. (a) M – H curve of Gd_2O_3 nanoparticles at $T = 300$ K [41]. (b) M – H curves of Ln_2O_3 nanoparticles, $Ln =$ (i) Tb and (ii) Ho at $T = 300$ K [43]. Net M values of Ln_2O_3 nanoparticles without ligands were used in the plots. Adapted from [41,43]. Copyrights 2020 and 2021 MDPI.

4.3. MR Imaging Properties: r_1 and r_2 Values

The r_1 and r_2 values are affected by the number of water molecules around the nanoparticles and the distance between them and, therefore, depend on the water-attracting ability of the ligands around the nanoparticles [59,60,65]. Accordingly, surface-coating ligands should be properly selected. Gd_2O_3 nanoparticles act as positive (T_1) MRI contrast agents due to the high spin magnetic moment of Gd^{3+} ($s = 7/2$); they have high r_1 values and r_2/r_1 ratios close to one [39–41] (T_1 MRI contrast agents exhibit low r_2/r_1 ratios, whereas T_2 MRI contrast agents have high r_2/r_1 ratios [23]). The r_1 and r_2 values of PAAMA-coated Gd_2O_3 nanoparticles at 3.0 T MR field were determined to be 40.6 and $63.4 \text{ s}^{-1} \text{ mM}^{-1}$ ($r_2/r_1 = 1.56$), respectively, using the $1/T_1$ and $1/T_2$ plots versus Gd-concentration depicted in Figure 9 [40]. This r_1 value is approximately 10 times higher than those [21–23] of commercial molecular T_1 MRI contrast agents, such as Dotarem, ProHance, Gadovist, Magnevist, and Omniscan [21,22]. The r_1 value also depends on the particle diameter of Gd_2O_3 nanoparticles, for which the optimal value was suggested to be 1.0 to 2.5 nm [24]. The observed particle diameter of the PAAMA-coated Gd_2O_3 nanoparticles is within this size range. As a reference, the r_1 and r_2 values of Gadovist as a commercial molecular agent are provided at the bottom of Figure 9, which shows that this nanoparticle sample is more powerful than Gadovist as a T_1 MRI contrast agent. On the other hand, other Ln_2O_3 nanoparticles ($Ln = Tb, Dy, \text{ and } Ho$) show appreciable to high r_2 values and negligible r_1 values with very large r_2/r_1 ratios [66]. Therefore, these nanoparticles are suitable as T_2 MRI contrast agents. The r_2 values of these nanoparticles increased with increasing the MR field [66] because r_2 is proportional M^2 [59,60]. Therefore, these nanoparticles are expected to provide appreciable T_2 MR contrast images at high MR fields. For example, PAA-coated Ln_2O_3 nanoparticles ($Ln = Tb \text{ and } Ho$) exhibit appreciable T_2 MR contrast images at 9.4 T MR Field [43]. For comparison, this T_2 contrast is lower than that of superparamagnetic iron oxide nanoparticles possessing high saturation magnetizations (50–80 emu/g) and high r_2 values [67,68].

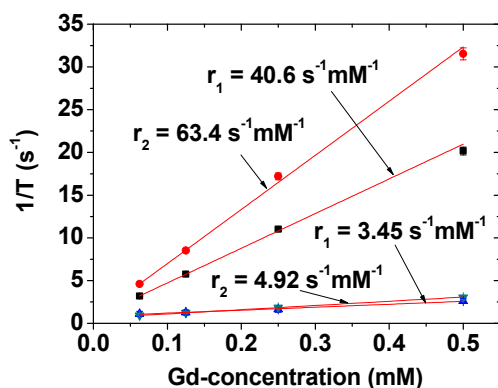


Figure 9. r_1 and r_2 values of PAAMA-coated Gd_2O_3 nanoparticles [40]. Adapted from [40]. Copyright 2021 MDPI.

5. In Vivo Imaging

5.1. Tumor-Targeting T_1 MRI Contrast Agents

Gd_2O_3 nanoparticles are the most widely applied Ln_2O_3 nanoparticles as in vivo tumor-targeting T_1 MRI contrast agents because of the high spin magnetic moment ($s = 7/2$) of Gd^{3+} ($^8S_{7/2}$), which is the largest value among the elements in the periodic table and thus provides very high T_1 MR contrast. Therefore, various studies on the synthesis and application of tumor-targeting Gd_2O_3 nanoparticles have been reported, which are discussed below according to the type of tumor-targeting ligands used.

5.1.1. Chlorotoxin (CTX)

Gu et al. developed a mouse brain tumor-targeting contrast agent using CTX as a tumor-targeting ligand [45]. CTX is a peptide consisting of a 36-amino acid sequence

found in the venom of the deathstalker scorpion [69]. CTX preferentially binds to glioma cells, enabling the development of therapeutic and diagnostic protocols for several types of tumors [70]. In this study, CTX-PEG-TETT-coated Gd_2O_3 nanoparticles with a core diameter of 3.46 nm and r_1 value of $8.41 \text{ s}^{-1} \text{ mM}^{-1}$ at 7.0 T were applied to tumor-targeting imaging in vivo. Figure 10 shows a series of in vivo T_1 MR images of mice with brain glioma tumor after mice tail intravenous injection of PEG-TETT- Gd_2O_3 and CTX-PEG-TETT- Gd_2O_3 nanoparticle samples at the same Gd dose (6 mg Gd/kg). The PEG-TETT- Gd_2O_3 nanoparticles slightly improved the contrast of glioma sites (labeled with arrows) compared with the preinjection image. However, the CTX-PEG-TETT- Gd_2O_3 nanoparticles exhibited highly enhanced T_1 MR images in brain tumors (labeled with arrows) after injection, clearly supporting that the CTX-PEG-TETT- Gd_2O_3 nanoparticles act as a tumor-targeting T_1 MRI contrast agent.

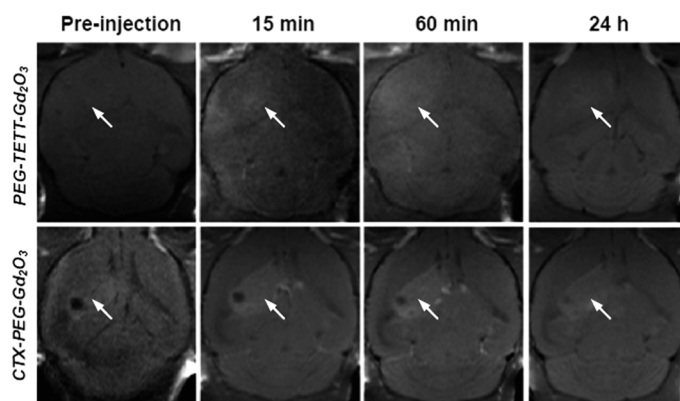


Figure 10. T_1 MR images of mice brains with C6 glioma before and after (15 min, 60 min, and 24 h) intravenous injection of PEG-TETT- Gd_2O_3 and CTX-PEG-TETT- Gd_2O_3 nanoparticle samples into mice tails at 7.0 T. Tumor sites are indicated with arrows. Adapted from [45]. Copyright 2014 The Royal Society of Chemistry.

5.1.2. Cyclic RGD (cRGD)

Ahmad et al. investigated Gd_2O_3 nanoparticles that were directly conjugated with cRGDs [47]. Prior to measuring in vivo T_1 MR images to confirm tumor targeting, an in vitro cellular incubation experiment was conducted with cRGD- Gd_2O_3 nanoparticles to confirm the internalization of the nanoparticles in the tumor cells, which is particularly important in the case of tumor theragnosis. To investigate this, human brain glioma (U87MG) tumor cells were incubated with cRGD- Gd_2O_3 nanoparticles (0.01 mM Gd). Untreated cells as a control group are shown in Figure 11a. The treated cells exhibited different surface morphologies from that of the control cells due to nanoparticle attachment on the tumor cell surfaces (Figure 11b). The internalization of cRGD- Gd_2O_3 nanoparticles in the tumor cells was confirmed by analyzing the TEM images of the cells, where no cRGD- Gd_2O_3 nanoparticles were found in the TEM image of the control cells (Figure 11c), whereas they were found in the treated tumor cells (Figure 11d). In addition, an energy-dispersive X-ray (EDX) spectroscopy analysis of the circled region in Figure 11d confirmed the presence of Gd (Figure 11e), supporting the internalization of cRGD- Gd_2O_3 nanoparticles in the U87MG tumor cells.

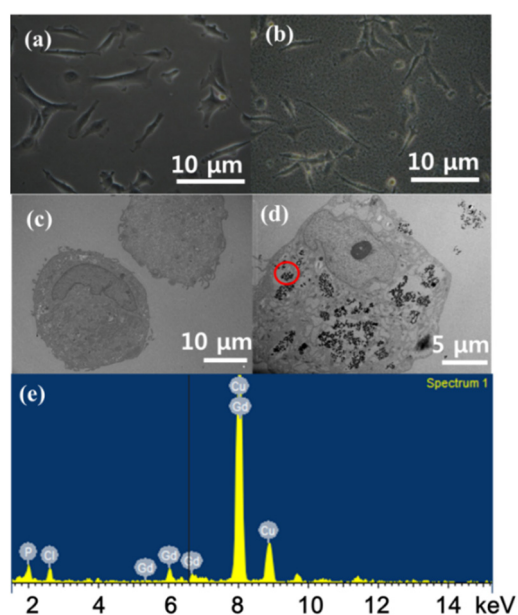


Figure 11. Optical microscope images of U87MG tumor cells incubated (a) without and (b) with cRGD-Gd₂O₃ nanoparticles. HRTEM images of U87MG tumor cells incubated (c) without and (d) with cRGD-Gd₂O₃ nanoparticles. (e) EDX spectrum of the circled region in (d). Adapted from [47]. Copyright 2018 Wiley.

To demonstrate the occurrence of *in vivo* tumor targeting via T₁ MRI, a sample solution containing cRGD-Gd₂O₃ nanoparticles was injected into the tail vein of a U87MG tumor-bearing mouse inoculated into the liver (injection dose = ~0.1 mmol Gd/kg) [47]. T₁ MR images were obtained before and after injection (Figure 12a). As shown in the figure, tumor targeting was confirmed via positive contrast enhancement in the liver tumor 5 min after injection, indicating the accumulation of the nanoparticles in the tumor. Figure 12b shows a color map of the middle T₁ MR image depicted in Figure 12a, in which the contrast enhancement in the liver tumor (i.e., the widely spread brighter part) can be clearly observed. The signal-to-noise ratios (SNRs) of the three regions of interest (ROIs) in the liver, i.e., the normal region (filled square), the tumor region (filled circle), and the necrotic region (filled triangle), as labeled in the inserted T₁ MR image, are plotted versus time in Figure 12c. The T₁ contrast enhancement in the liver tumor was approximately three times higher than in the normal region of the liver, as shown in the percentage SNR plots in Figure 12d. These results suggest that the cRGD-Gd₂O₃ nanoparticles act as a tumor-targeting T₁ MRI contrast agent.

5.1.3. TAT Peptide

Ahmad et al. explored the tumor-imaging application of transactivator of transcription (TAT) peptide-conjugated Gd₂O₃ nanoparticles [48]. The TAT peptide, which contains 48–57 fragments of the basic domain of the human immunodeficiency virus type 1 TAT protein, exhibits cell-penetrating properties [71]. To date, various nanomaterials grafted with TAT peptides have been applied in gene delivery, drug delivery, and tumor-cell imaging [72–74]. Ahmad et al. observed a greater accumulation of TAT peptide-grafted Gd₂O₃ nanoparticles in tumor cells than in normal cells in a mouse via T₁ MRI *in vivo* [48]. The TAT peptide allowed cell penetration of the nanoparticles during circulation through angiogenesis via the EPR effect [26,75].

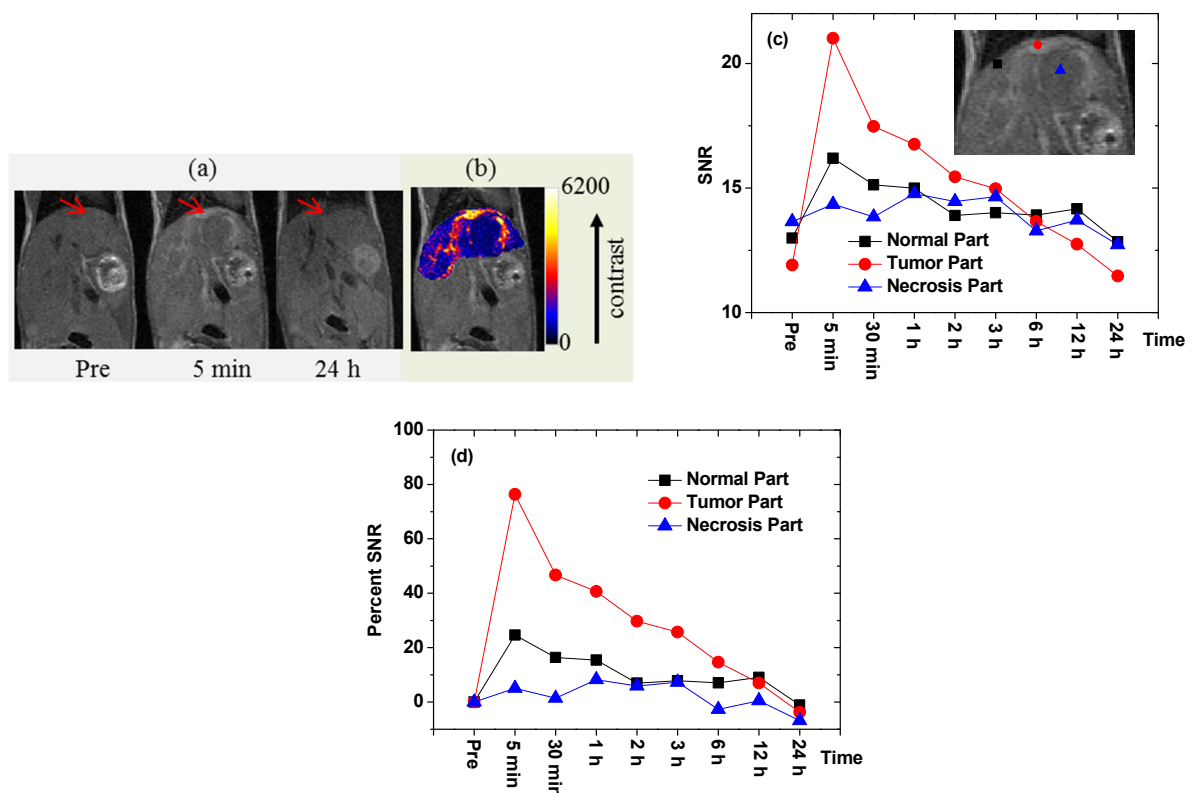


Figure 12. (a) T_1 MR images of a U87MG tumor-bearing nude mouse in the liver before and after intravenous injection (arrows indicate the tumor region). (b) Color map of the middle T_1 MR image in (a), showing the widely spread liver tumor (brighter region). (c) Plots of the SNRs of the ROIs in the normal, tumor, and necrosis parts of the liver versus time. (d) Plots of the percentage SNRs in the normal, tumor, and necrosis parts of the liver versus time; percentage SNR = $\{[\text{SNR}(\text{time}) - \text{SNR}(\text{Pre})] / \text{SNR}(\text{Pre})\} \times 100$. Adapted from [47]. Copyright 2018 Wiley.

5.1.4. Linear RGD

Recently, Ho et al. synthesized highly stable Gd_2O_3 nanoparticles coated with PAA and then conjugated with linear RGD (Figure 2) to target tumors by binding to $\alpha_v\beta_3$ and $\alpha_v\beta_5$ integrins, which are overexpressed in tumor angiogenic sites and tumor cells [44]. The RGD-PAA- Gd_2O_3 nanoparticles accumulated at the tumor sites, showing enhanced T_1 contrast at the tumor sites after injection (Figure 13). This result was probably due to the combination of various outstanding properties of the RGD-PAA- Gd_2O_3 nanoparticles, such as the delivery of hundreds of Gd atoms per nanoparticle to the tumor site, tumor-targeting ability, and ultrasmall size, which provides them with good transport properties during circulation through blood vessels and tumor-cell penetration. This study indicated that the RGD-PAA- Gd_2O_3 nanoparticles are applicable to in vivo tumor diagnosis.

5.2. MRI-Guided Therapy

One of the main advantages of Gd_2O_3 nanoparticles as T_1 MRI contrast agents is that they can be used for MRI-guided therapy. For example, Le Duc et al. developed gadolinium-based nanoparticles encapsulated in a polysiloxane shell and then grafted with diethylenetriaminepentaacetic dianhydride for nanoparticle colloidal stabilization [76]. They used the nanoparticles for tumor therapy using X-ray microbeam radiation [77,78], which improved the survival of mice against an aggressive brain tumor. The efficacy of this treatment depended on how accurately MRI contrast agents locate the tumor position and shape. In the T_1 MR images recorded a few minutes after intravenous injection, the delineation of the tumor was clearly distinguished from normal tissues in a rat brain as

shown in Figure 14, and X-ray microbeam radiation was then conducted to kill the brain tumor cells.

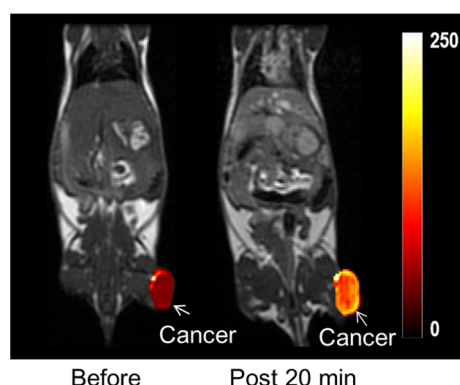


Figure 13. T₁ MR images before and 20 min after (labeled “post 20 min”) intravenous injection into the mouse tail: the bright contrast at the tumor (labeled with arrows) was due to the accumulation of nanoparticles at the tumor site. Adapted from [44]. Copyright 2020 The Royal Society of Chemistry.

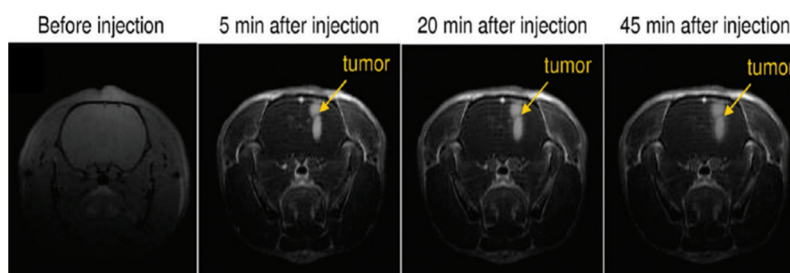


Figure 14. T₁-weighted images of the brain of a rat having intracerebral 9L gliosarcoma (9LGS) before and after (5, 20, and 45 min) intravenous injection of gadolinium-based nanoparticles. Adapted from [76]. Copyright 2011 American Chemical Society.

5.3. T₂-Weighted MRI

Recently, Ln₂O₃ (Ln = Tb, Dy, and Ho) nanoparticles with appreciable r_2 and negligible r_1 values, suitable for T₂ MRI were developed [42,43,50,66,79,80]. For example, PAA-coated Ln₂O₃ (Ln = Tb and Ho) nanoparticles exhibited appreciable r_2 values at 3.0 T MR field ($3.19 \text{ s}^{-1} \text{ mM}^{-1}$ for Ln = Tb and $1.44 \text{ s}^{-1} \text{ mM}^{-1}$ for Ln = Ho), enhanced r_2 values at 9.4 T MR field ($16.40 \text{ s}^{-1} \text{ mM}^{-1}$ for Ln = Tb and $9.20 \text{ s}^{-1} \text{ mM}^{-1}$ for Ln = Ho) [43], and negligible r_1 values at all MR fields. With such r_1 and r_2 values, only the exclusive induction of T₂ relaxations by the nanoparticles occurs at all MR fields. The appreciable T₂ MR contrast enhancements at 9.4 T MR field confirmed the effectiveness of the nanoparticles as T₂ MRI contrast agents at high MR fields in vivo [43]. Dy₂O₃ nanoparticles constitute another example with application in T₂ MRI. Thus, D-glucuronic acid-coated Dy₂O₃ nanoparticles exhibited T₂ MR contrast enhancements in a mouse liver at 3.0 T MR field in vivo [79] (Figure 15a), proving the potential of Dy₂O₃ nanoparticles as T₂ MRI contrast agents. Recently, Yue et al. investigated carbon-coated Dy₂O₃ nanoparticles as a new class of T₂ MRI contrast agent at 3.0 T MR field [80]. The nanoparticles were nearly non-toxic via an in vitro cellular cytotoxicity assay. The presence of numerous hydroxyl groups on the carbon-coating layer conferred the colloidal nanoparticles with stability in aqueous media. The nanoparticles exhibited T₂ contrast enhancement in the mice kidneys after intravenous administration, acting as a T₂ MRI contrast agent (Figure 15b).

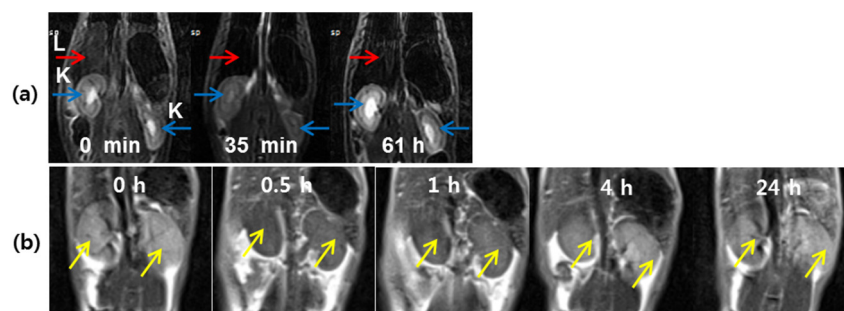


Figure 15. (a) A series of 3.0 T in vivo T_2 MR images: coronal views of kidneys and liver (labeled as “K” and “L”, respectively) before and after intravenous injection of an aqueous solution of D-glucuronic acid-coated Dy_2O_3 nanoparticles into the mouse tail [79]. (b) In vivo coronal 3.0 T T_2 MR images of the mice kidneys (indicated with arrows) as a function of time before and after intravenous injection of an aqueous solution of carbon-coated Dy_2O_3 nanoparticles into the mouse tail [80]. Adapted from [79,80]. Copyrights 2012 Elsevier and 2020 MDPI.

5.4. CT Imaging

Lanthanide elements exhibit higher X-ray attenuation coefficients [16] than iodine, which is currently used as a CT contrast agent in its organic molecular forms. Consequently, Ln_2O_3 nanoparticles can be applied as CT contrast agents [17,18,81,82]. For example, an aqueous solution of Gd_2O_3 nanoparticles coated with iodine compounds was used to investigate CT imaging in vivo [81]. Brighter contrast enhancements were observed in mouse bladder (labeled B in Figure 16a) after intravenous tail injection. The X-ray absorption in the ROI of the bladder (indicated by a small, dotted circle in Figure 16a) indicated that the contrast reached a maximum at ~ 30 min after injection and then decreased with time (Figure 16b), suggesting that the sample solution was excreted through the bladder as urine. This result showed that an aqueous solution of Gd_2O_3 nanoparticles might serve as a CT contrast agent.

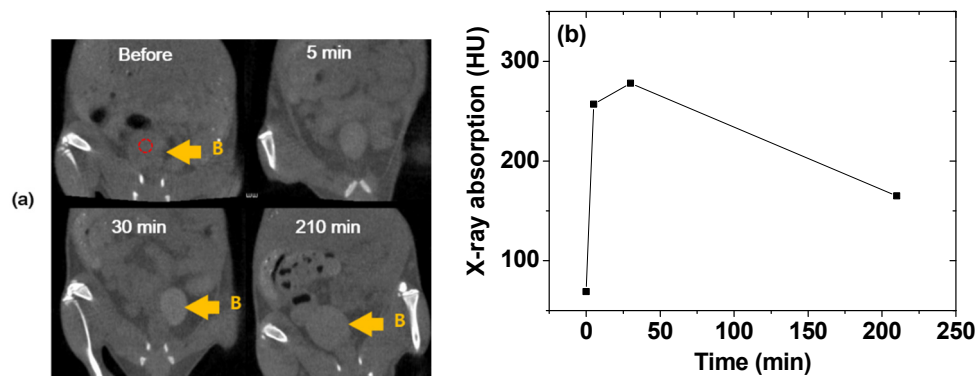


Figure 16. (a) In vivo CT images of a mouse bladder (labeled B) and (b) plot of the X-ray absorption of the ROI in the bladder (indicated by the small, dotted circle in (a)) before and after intravenous injection of an aqueous sample into the mouse tail [81]. Adapted from [81]. Copyright 2015 Springer Nature.

6. Ln_2O_3 Nanoparticle Toxicity

As shown in Figure 17a, bare Gd_2O_3 nanoparticles exhibit toxicities in both NCTC1469 normal and U87MG tumor-cell lines, whereas PAA-coated Gd_2O_3 nanoparticles are nearly non-toxic up to 500 μM Gd with cell viabilities of $\sim 93\%$ in DU145, $\sim 99\%$ in NCTC1469, and $\sim 80\%$ in U87MG cell lines (Figure 17b) [83]. Other PAA-coated Ln_2O_3 nanoparticles ($Ln = Dy, Tb,$ and Ho) also exhibit very low cytotoxicities in both DU145 and NCTC1469 cell lines (Figure 17c–e) [42,43], showing good biocompatibilities. These examples demonstrate

that Ln_2O_3 nanoparticles must be well protected with water-soluble and biocompatible ligands for biomedical applications.

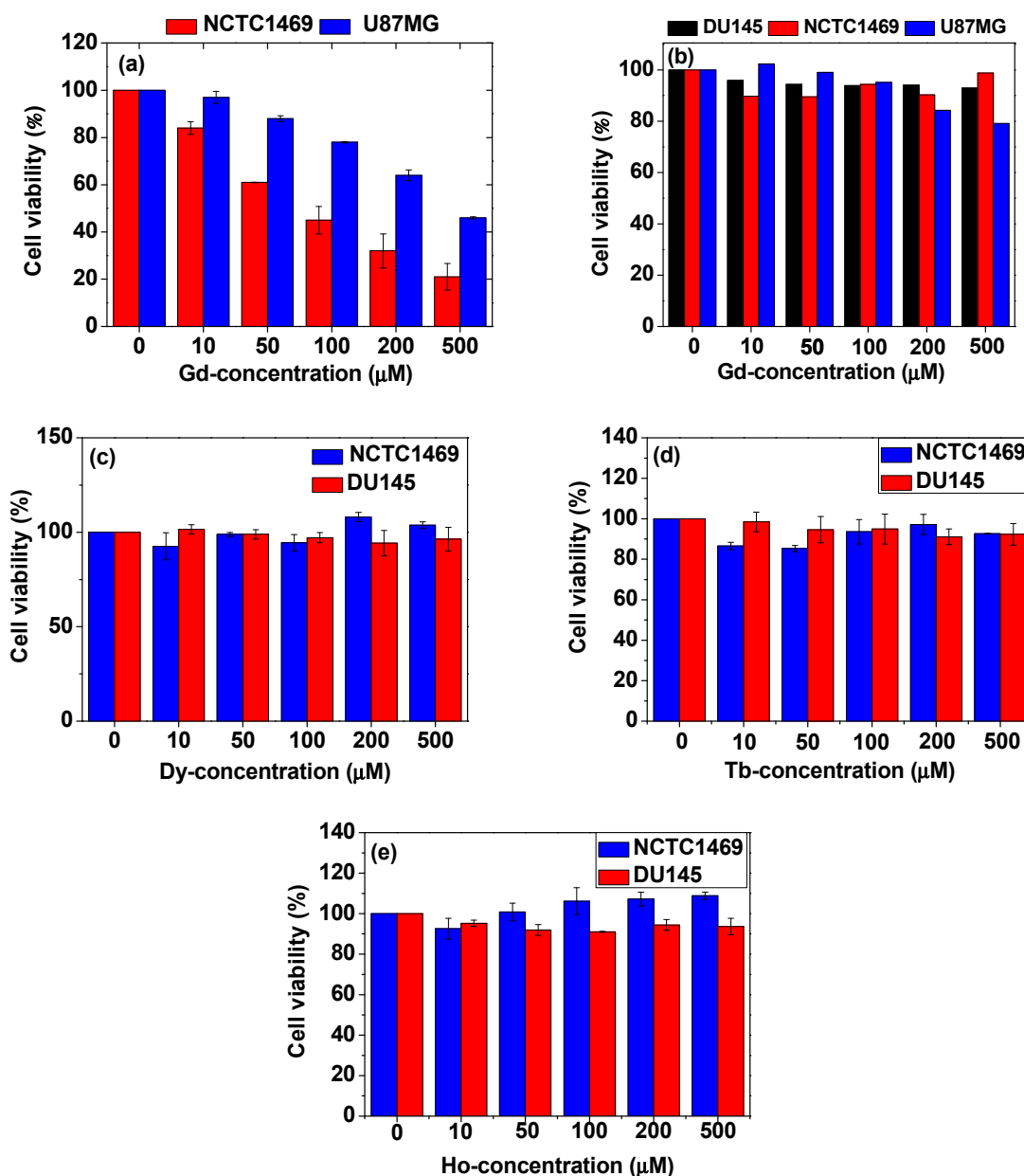


Figure 17. In vitro cytotoxicities of (a) uncoated Gd_2O_3 nanoparticles in NCTC1469 and U87MG cell lines and (b) PAA-coated Gd_2O_3 nanoparticles in DU145, NCTC1469, and U87MG cell lines [83]. PAA-coated Ln_2O_3 nanoparticles (Ln = (c) Dy, (d) Tb, and (e) Ho) in DU145 and NCTC1469 cell lines [42,43]. Adapted from [42,43,83]. Copyrights 2018, 2020 and 2021 The Royal Society of Chemistry, Wiley & MDPI.

Lanthanides are relatively non-toxic elements [37,38]. For example, for lanthanide chlorides, the lethal dose causing the death of 50% of a group of 10 animals (LD50) is higher than 10 and 450 mg per kg bodyweight for intravenous and intraperitoneal injections, respectively [84]. In the case of Ln_2O_3 nanoparticles, other properties, either alone or in concert, must be considered to evaluate the possible toxic effects of the nanoparticles. These properties include chemical composition, doping, hydrodynamic size, shape, redox properties, tendency for aggregation, composition of the shell or coating material, surface modifications, colloidal stability, solubility, biodegradability, concentration, and duration of exposure [85]. Although several studies have investigated the toxicity of lanthanide-based

nanoparticles having different properties, such as chemical composition, size, surface ligands, and lanthanide concentration [86–88], the lack of literature data has prevented drawing firm conclusions for the assessment of the potential toxicity of Ln_2O_3 nanoparticles. Furthermore, several aspects of the biological interaction of Ln_2O_3 nanoparticles in living systems still need to be unveiled. For example, despite *in vitro* cytotoxicity studies being conducted using various cell cultures, these studies did not provide information about long-term safety and cytotoxicity [89,90], for which *in vivo* cytotoxicity studies would be needed.

Nevertheless, several important conclusions can be extracted from the currently available literature data. In the case of biomedical applications, Ln_2O_3 nanoparticles are usually introduced into the body by intravenous injections and circulated by the bloodstream primarily to organs, such as the liver and spleen, kidneys, heart, lungs, and brain [91]. The possible retention or uptake in blood and organs strongly depends on the surface properties of the nanoparticles. Ligand coating can promote the interaction of the Ln_2O_3 nanoparticles with the cell membranes, favoring the internalization of the nanoparticles by various types of cells. However, biologically inert coating ligands, such as PEG, may prolong the circulation in the bloodstream of nanoparticles [11]. In addition, nanoparticle size is an important factor for the excretion route [92,93]. Thus, nanoparticles smaller than 3 nm can be excreted by renal filtration [19,20], whereas those larger than 3 nm are enclosed by a phagocyte system. As a part of the immune system, the phagocyte system is composed of several types of phagocytic cells in the reticular tissue within the body, whose main function is to remove undesired species, such as bacteria, viruses, and foreign materials, including nanoparticles.

The toxicity of Ln_2O_3 nanoparticles differs depending on the lanthanide ions. For example, Er_2O_3 shows higher toxicity than Gd_2O_3 and La_2O_3 and is highly toxic to zebrafish embryos at a concentration of 50 ppm Er, causing significant mortality and morphological malformations [93]. Meanwhile, the toxicity of Gd_2O_3 nanoparticles is primarily attributed to the release of Gd^{3+} ions [94–96]. The toxicity of Gd^{3+} ions has been addressed not only for Gd_2O_3 nanoparticles but also for a variety of molecular Gd^{3+} -chelates. In the case of Gd_2O_3 nanomaterials, Eu^{3+} -doped Gd_2O_3 ($\text{Gd}_2\text{O}_3:\text{Eu}^{3+}$) nanotubes can adversely affect bone marrow stromal cells (BMSCs) [97]. Yang et al. reported the application of ^{153}Sm -doped $\text{Gd}(\text{OH})_3$ nanorods as a potential MRI contrast agent [98]. *In vitro* cell toxicity tests revealed that $\text{Gd}(\text{OH})_3$ nanorods have no toxic effect on cellular proliferation and viability. Furthermore, an *in vivo* toxicity test using Kunming mice showed that injection up to 100 mg/kg of $\text{Gd}(\text{OH})_3$ nanorods had no toxic effect up to 150 days after exposure. However, this *in vivo* test investigated the short-term toxic effect of $\text{Gd}(\text{OH})_3$ nanorods. In contrast, the long-term toxicity of clinically used Gd^{3+} -chelates was reported. When used in patients with severely compromised kidney function, Gd^{3+} -chelates promoted the development of nephrogenic systemic fibrosis (NSF), which is a rare disease affecting different parts of the body that can lead to thickening or hardening of the skin and deposits [99] (Figure 18). Moreover, NSF is a progressive condition that can be fatal because it may cause multiple organ failure [99–102]. Gd^{3+} retention in the body, which is greater with linear structured Gd^{3+} -chelates than with macrocyclic structured Gd^{3+} -chelates, was demonstrated to be associated with NSF.

Compared with clinically used Gd^{3+} -chelates, the toxicity of Ln_2O_3 nanoparticles, including Gd_2O_3 nanoparticles, has been less explored. For instance, the extent, mechanism, chemical form, and clinical implications of chronic lanthanide retention for Ln_2O_3 nanoparticles remain unknown. Therefore, more comprehensive investigations are required to improve our understanding of Ln_2O_3 nanoparticle toxicity and its clinical importance. In this context, the development of new experimental techniques may play a significant role in unveiling lanthanide nanotoxicity. For example, nanotoxicogenomics [103], which uses DNA microarray technologies to investigate the impact of nanoparticles on global gene expression profiles of cells and tissues, has emerged as a new field of toxicology to provide new and important insights into the toxicity of Ln_2O_3 nanoparticles.

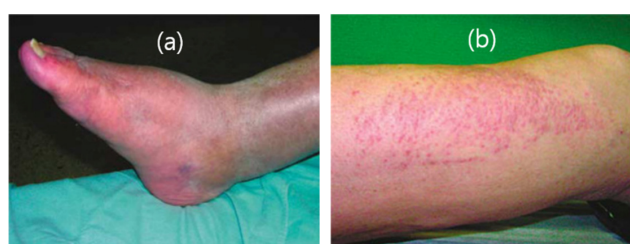


Figure 18. Clinical pictures of the legs of two patients with NSF for (a) about three years and (b) four weeks. Adapted from [99]. Copyright 2007 International Society of Nephrology.

7. Conclusions and Perspectives

Recent studies on the synthesis, surface modification, tumor-targeting ligand conjugation, toxicity, and novel biomedical applications to tumor-targeting T_1 MRI and image-guided tumor therapy of Ln_2O_3 nanoparticles were reviewed here. In addition, T_2 MRI and CT imaging applications were also discussed. High-quality Ln_2O_3 nanoparticles can be synthesized via the polyol method and organic-phase thermal decomposition method and then surface-coated with hydrophilic and biocompatible ligands for colloidal stability and biocompatibility. Polymers are more efficient than small molecules as surface-coating ligands because of their many $-\text{COOH}$, $-\text{NH}_2$, $-\text{OH}$ groups, which can be attached to nanoparticles and conjugated with tumor-targeting ligands and drugs.

The interest in Ln_2O_3 nanoparticles in the field of medical imaging lies principally in the excellent imaging properties of lanthanides, which arises from their appreciable paramagnetic moments at room temperature; Gd^{3+} has the highest 4f-electron spin magnetic moment ($s = 7/2$) among the elements in the periodic table, which is extremely useful for T_1 MRI, and other Ln^{3+} ions ($\text{Ln} = \text{Tb}$, Dy , and Ho) have a very high 4f-electron spin-orbital magnetic moment, which is suitable for T_2 MRI. In addition, lanthanide elements possess higher X-ray attenuation coefficients than iodine, which is currently used as a CT contrast agent in its organic compound forms. The potential of Ln_2O_3 nanoparticles as CT contrast agents has been confirmed by recording *in vivo* CT images. In the case of tumor targeting, Gd_2O_3 nanoparticles are the most widely investigated Ln_2O_3 nanoparticles due to their very high T_1 MRI sensitivity. Various tumor-targeting ligands have been conjugated to Gd_2O_3 nanoparticles for tumor imaging and T_1 MRI-guided tumor therapy. Especially, the enhanced accumulation of tumor-targeting ligand-coated Gd_2O_3 nanoparticles at tumor cells compared with that at normal cells allowed the development of precise image-guided tumor therapies via clear distinction and delineation of tumors from normal tissues.

As reviewed here, further intensive research is essential to achieve the ultimate goal of using Ln_2O_3 nanoparticles for tumor-targeting diagnosis and therapy and nontumor-targeting medical imaging. In addition, sophisticated toxicological and pharmacological improvements are required to demonstrate the safety of nanoparticle formulations prior to clinical trials. We hope that this review will guide the future development of biomedical applications of Ln_2O_3 nanoparticles.

Author Contributions: Conceptualization, M.Y.A., H.Y., T.T., S.L., S.L.H., G.H.L., S.-W.N. and Y.C.; investigation, M.Y.A., H.Y., T.T., S.L., S.L.H., G.H.L., S.-W.N. and Y.C.; writing—original draft preparation, M.Y.A.; writing—review and editing, G.H.L. and Y.C.; funding acquisition, G.H.L., Y.C. and S.-W.N. All authors have read and agreed to the published version of the manuscript.

Funding: This work was supported by the Basic Science Research Program of the National Research Foundation (NRF) funded by the Ministry of Education, Science, and Technology (No. 2016R1D1A3B01007622) and the Korean government (Ministry of Science, and Information and Communications Technology: MSIT) (No. 2021R1A4A1029433).

Informed Consent Statement: Not applicable.

Data Availability Statement: Not applicable.

Conflicts of Interest: The authors declare no conflict of interest.

References

1. García-Figueiras, R.; Baleato-González, S.; Padhani, A.; Luna-Alcalá, A.; Vallejo-Casas, J.A.; Sala, E.; Vilanova, J.C.; Koh, D.-M.; Herranz-Carnero, M.; Vargas, H.A. How clinical imaging can assess cancer biology. *Insights Imaging* **2019**, *10*, 1–35. [CrossRef]
2. Lecouvet, F.E. Whole-Body MR Imaging: Musculoskeletal Applications. *Radiology* **2016**, *279*, 345–365. [CrossRef]
3. Morone, M.; Bali, M.A.; Tunariu, N.; Messiou, C.; Blackledge, M.; Grazioli, L.; Koh, D.-M. Whole-Body MRI: Current Applications in Oncology. *Am. J. Roentgenol.* **2017**, *209*. [CrossRef]
4. Thakor, A.S.; Jokerst, J.V.; Ghanouni, P.; Campbell, J.L.; Mittra, E.; Gambhir, S.S. Clinically Approved Nanoparticle Imaging Agents. *J. Nucl. Med.* **2016**, *57*, 1833–1837. [CrossRef]
5. Kim, J.; Lee, N.; Hyeon, T. Recent development of nanoparticles for molecular imaging. *Philos. Trans. R. Soc. A Math. Phys. Eng. Sci.* **2017**, *375*, 20170022. [CrossRef]
6. Ehlerding, E.B.; Grodzinski, P.; Cai, W.; Liu, C.H. Big Potential from Small Agents: Nanoparticles for Imaging-Based Companion Diagnostics. *ACS Nano* **2018**, *12*, 2106–2121. [CrossRef] [PubMed]
7. Crist, R.M.; Dasa, S.S.K.; Liu, C.H.; Clogston, J.D.; Dobrovolskaia, M.A.; Stern, S.T. Challenges in the development of nanoparticle-based imaging agents: Characterization and biology. *Wiley Interdiscip. Rev. Nanomed. Nanobiotechnol.* **2020**, *13*. [CrossRef]
8. Sanità, G.; Carrese, B.; Lamberti, A. Nanoparticle Surface Functionalization: How to Improve Biocompatibility and Cellular Internalization. *Front. Mol. Biosci.* **2020**, *7*. [CrossRef]
9. Thiruppathi, R.; Mishra, S.; Ganapathy, M.; Padmanabhan, P.; Gulyás, B. Nanoparticle Functionalization and Its Potentials for Molecular Imaging. *Adv. Sci.* **2016**, *4*, 1600279. [CrossRef]
10. Ye, H.; Shen, Z.; Yu, L.; Wei, M.; Huilin, Y. Manipulating nanoparticle transport within blood flow through external forces: An exemplar of mechanics in nanomedicine. *Proc. R. Soc. A Math. Phys. Eng. Sci.* **2018**, *474*, 20170845. [CrossRef] [PubMed]
11. Suk, J.S.; Xu, Q.; Kim, N.; Hanes, J.; Ensign, L.M. PEGylation as a strategy for improving nanoparticle-based drug and gene delivery. *Adv. Drug Deliv. Rev.* **2015**, *99*, 28–51. [CrossRef] [PubMed]
12. Yue, H.; Park, J.Y.; Chang, Y.; Lee, G.H. Ultrasmall Europium, Gadolinium, and Dysprosium Oxide Nanoparticles: Polyol Synthesis, Properties, and Biomedical Imaging Applications. *Mini-Rev. Med. Chem.* **2020**, *20*, 1767–1780. [CrossRef] [PubMed]
13. Xu, W.; Kattel, K.; Park, J.Y.; Chang, Y.; Kim, T.J.; Lee, G.H. Paramagnetic nanoparticle T1 and T2 MRI contrast agents. *Phys. Chem. Chem. Phys.* **2012**, *14*, 12687–12700. [CrossRef]
14. Dong, H.; Du, S.-R.; Zheng, X.-Y.; Lyu, G.-M.; Sun, L.-D.; Li, L.-D.; Zhang, P.-Z.; Zhang, C.; Yan, C.-H. Lanthanide Nanoparticles: From Design toward Bioimaging and Therapy. *Chem. Rev.* **2015**, *115*, 10725–10815. [CrossRef]
15. Xu, W.; Chang, Y.; Lee, G.H. Biomedical Applications of Lanthanide Oxide Nanoparticles. *J. Biomater. Tissue Eng.* **2017**, *7*, 757–769. [CrossRef]
16. Hubbell, J.H.; Seltzer, S.M. *Tables of X-Ray Mass Attenuation Coefficients and Mass Energy-Absorption Coefficients from 1 keV to 20 MeV for Elements Z = 1 to 92 and 48 Additional Substances of Dosimetric Interest*; NIST: Gaithersburg, MD, USA, 1996. Available online: <http://www.nist.gov/pml/data/xraycoef> (accessed on 1 July 2021).
17. Ghazanfari, A.; Marasini, S.; Miao, X.; Park, J.A.; Jung, K.-H.; Ahmad, M.Y.; Yue, H.; Ho, S.L.; Liu, S.; Jang, Y.J.; et al. Synthesis, characterization, and X-ray attenuation properties of polyacrylic acid-coated ultrasmall heavy metal oxide (Bi₂O₃, Yb₂O₃, NaTaO₃, Dy₂O₃, and Gd₂O₃) nanoparticles as potential CT contrast agents. *Colloids Surfaces A Physicochem. Eng. Asp.* **2019**, *576*, 73–81. [CrossRef]
18. Lee, E.J.; Heo, W.C.; Park, J.W.; Chang, Y.; Bae, J.-E.; Chae, K.S.; Kim, T.J.; Park, J.A.; Lee, G.H. D-Glucuronic Acid Coated Gd(IO₃)₃·2H₂O Nanomaterial as a Potential T1MRI-CT Dual Contrast Agent. *Eur. J. Inorg. Chem.* **2013**, *2013*, 2858–2866. [CrossRef]
19. Xu, J.; Peng, C.; Yu, M.; Zheng, J. Renal clearable noble metal nanoparticles: Photoluminescence, elimination, and biomedical applications. *Wiley Interdiscip. Rev. Nanomed. Nanobiotechnol.* **2017**, *9*, e1453. [CrossRef] [PubMed]
20. Du, B.; Yu, M.; Zheng, J. Transport and interactions of nanoparticles in the kidneys. *Nat. Rev. Mater.* **2018**, *3*, 358–374. [CrossRef]
21. Hermann, P.; Kotek, J.; Kubíček, V.; Lukeš, I. Gadolinium(III) complexes as MRI contrast agents: Ligand design and properties of the complexes. *Dalton Trans.* **2008**, 3027–3047. [CrossRef] [PubMed]
22. Chan, K.W.-Y.; Wong, W.-T. Small molecular gadolinium(III) complexes as MRI contrast agents for diagnostic imaging. *Co-Ord. Chem. Rev.* **2007**, *251*, 2428–2451. [CrossRef]
23. Wahsner, J.; Gale, E.M.; Rodríguez-Rodríguez, A.; Caravan, P. Chemistry of MRI Contrast Agents: Current Challenges and New Frontiers. *Chem. Rev.* **2018**, *119*, 957–1057. [CrossRef] [PubMed]
24. Park, J.Y.; Baek, M.J.; Choi, E.S.; Woo, S.; Kim, J.H.; Kim, T.J.; Jung, J.C.; Chae, K.S.; Chang, Y.; Lee, G.H. Paramagnetic Ultrasmall Gadolinium Oxide Nanoparticles as Advanced T1 MRI Contrast Agent: Account for Large Longitudinal Relaxivity, Optimal Particle Diameter, and In Vivo T1 MR Images. *ACS Nano* **2009**, *3*, 3663–3669. [CrossRef]
25. Cho, M.; Sethi, R.; Narayanan, J.S.A.; Lee, S.S.; Benoit, D.N.; Taheri, N.; Decuzzi, P.; Colvin, V.L. Gadolinium oxide nanoplates with high longitudinal relaxivity for magnetic resonance imaging. *Nanoscale* **2014**, *6*, 13637–13645. [CrossRef] [PubMed]
26. Tee, J.K.; Yip, L.X.; Tan, E.S.; Santitewagun, S.; Prasath, A.; Ke, P.C.; Ho, H.K.; Leong, D.T. Nanoparticles' interactions with vasculature in diseases. *Chem. Soc. Rev.* **2019**, *48*, 5381–5407. [CrossRef]
27. Danhier, F.; Le Breton, A.; Pr at, V. RGD-Based Strategies To Target Alpha(v) Beta(3) Integrin in Cancer Therapy and Diagnosis. *Mol. Pharm.* **2012**, *9*, 2961–2973. [CrossRef]
28. Zhou, Q.-H.; You, Y.-Z.; Wu, C.; Huang, Y.; Oupický, D. Cyclic RGD-targeting of reversibly stabilized DNA nanoparticles enhances cell uptake and transfection in vitro. *J. Drug Target.* **2009**, *17*, 364–373. [CrossRef] [PubMed]

29. Boturyn, D.; Dumy, P. Tumor Targeting with RGD Peptide Ligands-Design of New Molecular Conjugates for Imaging and Therapy of Cancers. *Anti-Cancer Agents Med. Chem.* **2007**, *7*, 552–558. [[CrossRef](#)]
30. Li, J.; Zheng, L.; Cai, H.; Sun, W.; Shen, M.; Zhang, G.; Shi, X. Polyethyleneimine-mediated synthesis of folic acid-targeted iron oxide nanoparticles for in vivo tumor MR imaging. *Biomaterials* **2013**, *34*, 8382–8392. [[CrossRef](#)]
31. Marasini, S.; Yue, H.; Ho, S.-L.; Park, J.-A.; Kim, S.; Yang, J.-U.; Cha, H.; Liu, S.; Tegafaw, T.; Ahmad, M.; et al. In Vivo Positive Magnetic Resonance Imaging of Brain Cancer (U87MG) Using Folic Acid-Conjugated Polyacrylic Acid-Coated Ultrasmall Manganese Oxide Nanoparticles. *Appl. Sci.* **2021**, *11*, 2596. [[CrossRef](#)]
32. Huang, R.; Han, L.; Li, J.; Liu, S.; Shao, K.; Kuang, Y.; Hu, X.; Wang, X.; Lei, H.; Jiang, C. Chlorotoxin-modified macromolecular contrast agent for MRI tumor diagnosis. *Biomaterials* **2011**, *32*, 5177–5186. [[CrossRef](#)]
33. Cohen, G.; Burks, S.R.; Frank, J.A. Chlorotoxin—A Multimodal Imaging Platform for Targeting Glioma Tumors. *Toxins* **2018**, *10*, 496. [[CrossRef](#)] [[PubMed](#)]
34. Zahavi, D.; Weiner, L. Monoclonal antibodies in cancer therapy. *Antibodies* **2020**, *9*, 34. [[CrossRef](#)] [[PubMed](#)]
35. Beck, A.; Goetsch, L.; Dumontet, C.; Corvaia, N. Strategies and challenges for the next generation of antibody–drug conjugates. *Nat. Rev. Drug Discov.* **2017**, *16*, 315–337. [[CrossRef](#)] [[PubMed](#)]
36. Bouchard, H.; Viskov, C.; Garcia-Echeverria, C. Antibody-drug conjugates-a new wave of cancer drugs. *Bioorg. Med. Chem. Lett.* **2014**, *24*, 5357–5363. [[CrossRef](#)]
37. Wells, W.H., Jr.; Wells, V.L. The lanthanides, rare earth metals. In *Patty's Toxicology*, 6th ed.; Bingham, E., Cohns, B., Eds.; John Wiley & Sons, Inc.: Berlin, Germany, 2012; Volume 1, pp. 817–840.
38. Malhotra, N.; Hsu, H.-S.; Liang, S.-T.; Roldan, M.J.M.; Lee, J.-S.; Ger, T.-R.; Hsiao, C.-D. An Updated Review of Toxicity Effect of the Rare Earth Elements (REEs) on Aquatic Organisms. *Animals* **2020**, *10*, 1663. [[CrossRef](#)]
39. Miao, X.; Ho, S.L.; Tegafaw, T.; Cha, H.; Chang, Y.; Oh, I.T.; Yaseen, A.M.; Marasini, S.; Ghazanfari, A.; Yue, H.; et al. Stable and non-toxic ultrasmall gadolinium oxide nanoparticle colloids (coating material = polyacrylic acid) as high-performance T1 magnetic resonance imaging contrast agents. *RSC Adv.* **2018**, *8*, 3189–3197. [[CrossRef](#)]
40. Jang, Y.J.; Liu, S.; Yue, H.; Park, J.A.; Cha, H.; Ho, S.L.; Marasini, S.; Ghazanfari, A.; Ahmad, M.Y.; Miao, X.; et al. Hydrophilic biocompatible poly(acrylic acid-co-maleic acid) polymer as a surface-coating ligand of ultrasmall Gd₂O₃ nanoparticles to obtain a high r1 value and T1 MR images. *Diagnostics* **2021**, *11*, 2. [[CrossRef](#)]
41. Ahmad, M.Y.; Ahmad, W.; Yue, H.; Ho, S.L.; Park, J.A.; Jung, K.-H.; Cha, H.; Marasini, S.; Ghazanfari, A.; Liu, S.; et al. In Vivo Positive Magnetic Resonance Imaging Applications of Poly(methyl vinyl ether-alt-maleic acid)-coated Ultra-small Paramagnetic Gadolinium Oxide Nanoparticles. *Molecules* **2020**, *25*, 1159. [[CrossRef](#)]
42. Marasini, S.; Yue, H.; Ho, S.L.; Cha, H.; Park, J.A.; Jung, K.; Ghazanfari, A.; Ahmad, M.Y.; Liu, S.; Chae, K.; et al. A Novel Paramagnetic Nanoparticle T2 Magnetic Resonance Imaging Contrast Agent with High Colloidal Stability: Polyacrylic Acid-Coated Ultrafine Dysprosium Oxide Nanoparticles. *Bull. Korean Chem. Soc.* **2020**, *41*, 829–836. [[CrossRef](#)]
43. Marasini, S.; Yue, H.; Ho, S.L.; Park, J.; Kim, S.; Jung, K.H.; Cha, H.; Liu, S.; Tegafaw, T.; Ahmad, M.Y.; et al. Synthesis, Characterizations, and 9.4 tesla T2 MR images of polyacrylic acid-coated terbium (III) and holmium (III) oxide nanoparticles. *Nanomaterials* **2021**, *11*, 1355. [[CrossRef](#)]
44. Ho, S.L.; Choi, G.; Yue, H.; Kim, H.-K.; Jung, K.-H.; Park, J.A.; Kim, M.H.; Lee, Y.J.; Kim, J.Y.; Miao, X.; et al. In vivo neutron capture therapy of cancer using ultrasmall gadolinium oxide nanoparticles with cancer-targeting ability. *RSC Adv.* **2020**, *10*, 865–874. [[CrossRef](#)]
45. Gu, W.; Song, G.; Li, S.; Shao, C.; Yan, C.; Ye, L. Chlorotoxin-conjugated, PEGylated Gd₂O₃ nanoparticles as a glioma-specific magnetic resonance imaging contrast agent. *RSC Adv.* **2014**, *4*, 50254–50260. [[CrossRef](#)]
46. Stoddart, M.J. *Mammalian Cell Viability, Methods and Protocols*; Humana Press: New York, NY, USA, 2011.
47. Ahmad, M.Y.; Ahmad, M.W.; Cha, H.; Oh, I.-T.; Tegafaw, T.; Miao, X.; Ho, S.L.; Marasini, S.; Ghazanfari, A.; Yue, H.; et al. Cyclic RGD-Coated Ultrasmall Gd₂O₃ Nanoparticles as Tumor-Targeting Positive Magnetic Resonance Imaging Contrast Agents. *Eur. J. Inorg. Chem.* **2018**, *2018*, 3070–3079. [[CrossRef](#)]
48. Ahmad, M.Y.; Cha, H.; Oh, I.T.; Tegafaw, T.; Miao, X.; Ho, S.L.; Marasini, S.; Ghazanfari, A.; Yue, H.; Chae, K.S.; et al. Synthesis, characterization, and enhanced cancer-Imaging application of trans-activator of transcription peptide-conjugated ultrasmall gadolinium oxide nanoparticles. *Bull. Korean Chem. Soc.* **2018**, *39*, 435–441. [[CrossRef](#)]
49. Söderlind, F.; Pedersen, H.; Petoral, R.M.; Käll, P.-O.; Uvdal, K. Synthesis and characterisation of Gd₂O₃ nanocrystals functionalised by organic acids. *J. Colloid Interface Sci.* **2005**, *288*, 140–148. [[CrossRef](#)]
50. Kattel, K.; Park, J.Y.; Xu, W.; Kim, H.G.; Lee, E.J.; Alam Bony, B.; Heo, W.C.; Lee, J.J.; Jin, S.; Baeck, J.S.; et al. A Facile Synthesis, In vitro and In vivo MR Studies of d-Glucuronic Acid-Coated Ultrasmall Ln₂O₃ (Ln = Eu, Gd, Dy, Ho, and Er) Nanoparticles as a New Potential MRI Contrast Agent. *ACS Appl. Mater. Interfaces* **2011**, *3*, 3325–3334. [[CrossRef](#)]
51. Heiba, Z.; Okuyucu, H.; Hascicek, Y.S. X-ray structure determination of the rare earth oxides (Er_{1-u}Gd)₂O₃ applying the Rietveld method. *J. Appl. Crystallogr.* **2002**, *35*, 577–580. [[CrossRef](#)]
52. Kattel, K.; Park, J.Y.; Xu, W.; Kim, H.G.; Lee, E.J.; Alam Bony, B.; Heo, W.C.; Chang, Y.; Kim, T.J.; Do, J.Y.; et al. Water-soluble ultrasmall Eu₂O₃ nanoparticles as a fluorescent imaging agent: In vitro and in vivo studies. *Colloids Surfaces A Physicochem. Eng. Asp.* **2012**, *394*, 85–91. [[CrossRef](#)]
53. Pearson, R.G. Hard and Soft Acids and Bases. *J. Am. Chem. Soc.* **1963**, *85*, 3533–3539. [[CrossRef](#)]
54. Pearson, R.G. Hard and soft acids and bases, HSAB, part 1: Fundamental principles. *J. Chem. Educ.* **1968**, *45*. [[CrossRef](#)]

55. Pearson, R.G. Hard and soft acids and bases, HSAB, part II: Underlying theories. *J. Chem. Educ.* **1968**, *45*, 643–648. [[CrossRef](#)]
56. Psarra, E.; König, U.; Müller, M.; Bittrich, E.; Eichhorn, K.-J.; Welzel, P.B.; Stamm, M.; Uhlmann, P. In Situ Monitoring of Linear RGD-Peptide Bioconjugation with Nanoscale Polymer Brushes. *ACS Omega* **2017**, *2*, 946–958. [[CrossRef](#)]
57. Yue, H.; Marasini, S.; Ahmad, M.Y.; Ho, S.L.; Cha, H.; Liu, S.; Jang, Y.J.; Tegafaw, T.; Ghazanfari, A.; Miao, X.; et al. Carbon-coated ultrasmall gadolinium oxide (Gd₂O₃@C) nanoparticles: Application to magnetic resonance imaging and fluorescence properties. *Colloids Surfaces A Physicochem. Eng. Asp.* **2019**, *586*, 124261. [[CrossRef](#)]
58. Corbierre, M.K.; Cameron, N.S.; Lennox, R.B. Polymer-Stabilized Gold Nanoparticles with High Grafting Densities. *Langmuir* **2004**, *20*, 2867–2873. [[CrossRef](#)]
59. Roch, A.; Gillis, P.; Muller, R.N. Theory of proton relaxation induced by superparamagnetic particles. *J. Chem. Phys.* **1999**, *110*, 5403–5411. [[CrossRef](#)]
60. Roch, A.; Gossuin, Y.; Muller, R.N.; Gillis, P. Superparamagnetic colloid suspensions: Water magnetic relaxation and clustering. *J. Magn. Magn. Mater.* **2005**, *293*, 532–539. [[CrossRef](#)]
61. Koehler, W.C.; Wollan, E.O.; Wilkinson, M.K. Paramagnetic and Nuclear Scattering Cross Sections of Holmium Sesquioxide. *Phys. Rev.* **1958**, *110*, 37–40. [[CrossRef](#)]
62. Wolf, W.P.; Meissner, H.; Catanese, C.A. Magnetic Properties of Rare Earth Hydroxides. *J. Appl. Phys.* **1968**, *39*, 1134–1136. [[CrossRef](#)]
63. Lal, H.B.; Pratap, V.; Kumar, A. Magnetic susceptibility of heavy rare-earth sesquioxides. *Pramana* **1978**, *10*, 409–412. [[CrossRef](#)]
64. Greenwood, N.N.; Earnshaw, A. *Chemistry of the Elements*, 2nd ed.; Butterworth-Heinemann: New York, NY, USA, 1997; p. 1243.
65. Marasini, S.; Yue, H.; Ghazanfari, A.; Ho, S.L.; Park, J.A.; Kim, S.; Cha, H.; Liu, S.; Tegafaw, T.; Ahmad, M.Y.; et al. Polyaspartic Acid-Coated Paramagnetic Gadolinium Oxide Nanoparticles as a Dual-Modal T₁ and T₂ Magnetic Resonance Imaging Contrast Agent. *Appl. Sci.* **2021**, *11*, 8222. [[CrossRef](#)]
66. Marasini, S.; Yue, H.; Ho, S.L.; Jung, K.-H.; Park, J.A.; Cha, H.; Ghazanfari, A.; Ahmad, M.Y.; Liu, S.; Jang, Y.J.; et al. D-glucuronic acid-coated ultrasmall paramagnetic Ln₂O₃ (Ln = Tb, Dy, and Ho) nanoparticles: Magnetic properties, water proton relaxivities, and fluorescence properties. *Eur. J. Inorg. Chem.* **2019**, *34*, 3832–3839. [[CrossRef](#)]
67. Zhao, Z.; Zhou, Z.; Bao, J.; Wang, Z.; Hu, J.; Chi, X.; Ni, K.; Wang, R.; Chen, X.; Chen, Z.; et al. Octapod iron oxide nanoparticles as high-performance T₂ contrast agents for magnetic resonance imaging. *Nat. Commun.* **2013**, *4*, 2266. [[CrossRef](#)] [[PubMed](#)]
68. Wei, R.; Zhou, T.; Sun, C.; Lin, H.; Yang, L.; Ren, B.W.; Chen, Z.; Gao, J. Iron-oxide-based twin nanoplates with strong T₂ relaxation shortening for contrast-enhanced magnetic resonance imaging. *Nanoscale* **2018**, *10*, 18398–18406. [[CrossRef](#)]
69. DeBin, J.; Strichartz, G. Chloride channel inhibition by the venom of the scorpion *Leiurus quinquestriatus*. *Toxicon* **1991**, *29*, 1403–1408. [[CrossRef](#)]
70. Deshane, J.; Garner, C.; Sontheimer, H. Chlorotoxin Inhibits Glioma Cell Invasion via Matrix Metalloproteinase-2. *J. Biol. Chem.* **2003**, *278*, 4135–4144. [[CrossRef](#)]
71. Debaisieux, S.; Rayne, F.; Yezid, H.; Beaumelle, B. The Ins and Outs of HIV-1 Tat. *Traffic* **2011**, *13*, 355–363. [[CrossRef](#)]
72. Pan, L.; He, Q.; Liu, J.; Chen, Y.; Ma, M.; Zhang, L.; Shi, J. Nuclear-Targeted Drug Delivery of TAT Peptide-Conjugated Monodisperse Mesoporous Silica Nanoparticles. *J. Am. Chem. Soc.* **2012**, *134*, 5722–5725. [[CrossRef](#)] [[PubMed](#)]
73. Peng, L.-H.; Niu, J.; Zhang, C.-Z.; Yu, W.; Wu, J.-H.; Shan, Y.-H.; Wang, X.-R.; Shen, Y.; Mao, Z.-W.; Liang, W.-Q.; et al. TAT conjugated cationic noble metal nanoparticles for gene delivery to epidermal stem cells. *Biomaterials* **2014**, *35*, 5605–5618. [[CrossRef](#)]
74. Santra, S.; Yang, H.; Dutta, D.; Stanley, J.T.; Holloway, P.H.; Tan, W.; Moudgil, B.M.; Mericle, R.A. TAT conjugated, FITC doped silica nanoparticles for bioimaging applications. *Chem. Commun.* **2004**, 2810–2811. [[CrossRef](#)]
75. Shi, Y.; Van Der Meel, R.; Chen, X.; Lammers, T. The EPR effect and beyond: Strategies to improve tumor targeting and cancer nanomedicine treatment efficacy. *Theranostics* **2020**, *10*, 7921–7924. [[CrossRef](#)]
76. Le Duc, G.; Miladi, I.; Alric, C.; Mowat, P.; Bräuer-Krisch, E.; Bouchet, A.; Khalil, E.; Bilottey, C.; Janier, M.; Lux, F.; et al. Toward an Image-Guided Microbeam Radiation Therapy Using Gadolinium-Based Nanoparticles. *ACS Nano* **2011**, *5*, 9566–9574. [[CrossRef](#)] [[PubMed](#)]
77. Laissue, J.A.; Geiser, G.; Spanne, P.O.; Dilmanian, F.A.; Gebbers, J.-O.; Geiser, M.; Wu, X.-Y.; Makar, M.S.; Micca, P.L.; Nawrocky, M.M.; et al. Neuropathology of ablation of rat gliosarcomas and contiguous brain tissues using a microplanar beam of synchrotron-wiggler-generated X rays. *Int. J. Cancer* **1998**, *78*, 654–660. [[CrossRef](#)]
78. Dilmanian, F.A.; Button, T.M.; Le Duc, G.; Zhong, N.; Pena, L.A.; Smith, J.A.L.; Martinez, S.R.; Bacarian, T.; Tammam, J.; Ren, B.; et al. Response of rat intracranial 9L gliosarcoma to microbeam radiation therapy. *Neuro-Oncology* **2002**, *4*, 26–38. [[CrossRef](#)] [[PubMed](#)]
79. Kattel, K.; Park, J.Y.; Xu, W.; Kim, H.G.; Lee, E.J.; Alam Bony, B.; Heo, W.C.; Jin, S.; Baek, J.S.; Chang, Y.; et al. Paramagnetic dysprosium oxide nanoparticles and dysprosium hydroxide nanorods as T₂ MRI contrast agents. *Biomaterials* **2012**, *33*, 3254–3261. [[CrossRef](#)]
80. Yue, H.; Park, J.; Ho, S.; Ahmad, M.; Cha, H.; Liu, S.; Tegafaw, T.; Marasini, S.; Ghazanfari, A.; Kim, S.; et al. New Class of Efficient T₂ Magnetic Resonance Imaging Contrast Agent: Carbon-Coated Paramagnetic Dysprosium Oxide Nanoparticles. *Pharmaceutics* **2020**, *13*, 312. [[CrossRef](#)]
81. Ahmad, M.W.; Xu, W.; Kim, S.J.; Baek, J.S.; Chang, Y.; Bae, J.E.; Chae, K.S.; Park, J.A.; Kim, T.J.; Lee, G.H. Potential dual imaging nanoparticle: Gd₂O₃ nanoparticle. *Sci. Rep.* **2015**, *5*, 8549. [[CrossRef](#)]

82. Cheung, E.N.M.; Alvares, R.D.A.; Oakden, W.; Chaudhary, R.; Hill, M.L.; Pichaandi, J.; Mo, G.C.H.; Yip, C.; Macdonald, P.M.; Stanisz, G.J.; et al. Polymer-Stabilized Lanthanide Fluoride Nanoparticle Aggregates as Contrast Agents for Magnetic Resonance Imaging and Computed Tomography. *Chem. Mater.* **2010**, *22*, 4728–4739. [[CrossRef](#)]
83. Ho, S.L.; Cha, H.; Oh, I.T.; Jung, K.-H.; Kim, M.H.; Lee, Y.J.; Miao, X.; Tegafaw, T.; Ahmad, M.Y.; Chae, K.S.; et al. Magnetic resonance imaging, gadolinium neutron capture therapy, and tumor cell detection using ultrasmall Gd₂O₃ nanoparticles coated with polyacrylic acid-rhodamine B as a multifunctional tumor theragnostic agent. *RSC Adv.* **2018**, *8*, 12653–12665. [[CrossRef](#)]
84. Hirano, S.; Suzuki, K.T. Exposure, metabolism, and toxicity of rare earths and related compounds. *Environ. Health Perspect.* **1996**, *104*, 85–95.
85. Nel, A.E.; Mädler, L.; Velegol, D.; Xia, T.; Hoek, E.M.V.; Somasundaran, P.; Klaessig, F.; Castranova, V.; Thompson, M. Understanding biophysicochemical interactions at the nano–bio interface. *Nat. Mater.* **2009**, *8*, 543–557. [[CrossRef](#)]
86. Jiang, W.; Kim, B.Y.; Rutka, J.T.; Chan, W.C.W. Nanoparticle-mediated cellular response is size-dependent. *Nat. Nanotechnol.* **2008**, *3*, 145–150. [[CrossRef](#)]
87. Lim, S.F.; Riehn, R.; Ryu, W.S.; Khanarian, N.; Tung, C.-K.; Tank, D.; Austin, R.H. In Vivo and Scanning Electron Microscopy Imaging of Upconverting Nanophosphors in *Caenorhabditis elegans*. *Nano Lett.* **2005**, *6*, 169–174. [[CrossRef](#)]
88. Chen, J.; Guo, C.; Wang, M.; Huang, L.; Wang, L.; Mi, C.; Li, J.; Fang, X.; Mao, C.; Xu, S. Controllable synthesis of NaYF₄: Yb, Er upconversion nanophosphors and their application to in vivo imaging of *Caenorhabditis elegans*. *J. Mater. Chem.* **2011**, *21*, 2632–2638. [[CrossRef](#)]
89. Gu, Z.; Yan, L.; Tian, G.; Li, S.; Chai, Z.; Zhao, Y. Recent Advances in Design and Fabrication of Upconversion Nanoparticles and Their Safe Theranostic Applications. *Adv. Mater.* **2013**, *25*, 3758–3779. [[CrossRef](#)]
90. Fadeel, B.; Garcia-Bennett, A.E. Better safe than sorry: Understanding the toxicological properties of inorganic nanoparticles manufactured for biomedical applications. *Adv. Drug Deliv. Rev.* **2010**, *62*, 362–374. [[CrossRef](#)] [[PubMed](#)]
91. Rogosnitzky, M.; Branch, S.M. Gadolinium-based contrast agent toxicity: A review of known and proposed mechanisms. *BioMetals* **2016**, *29*, 365–376. [[CrossRef](#)]
92. Gnach, A.; Lipinski, T.; Bednarkiewicz, A.; Rybka, J.; Capobianco, J.A. Upconverting nanoparticles: Assessing the toxicity. *Chem. Soc. Rev.* **2014**, *44*, 1561–1584. [[CrossRef](#)]
93. Harper, S.; Usenko, C.; Hutchison, J.E.; Maddux, B.L.S.; Tanguay, R.L. Biodistribution and toxicity depends on nanomaterial composition, size, surface functionalisation and route of exposure. *J. Exp. Nanosci.* **2008**, *3*, 195–206. [[CrossRef](#)]
94. Tweedle, M.F. Gadolinium deposition: Is it chelated or dissociated gadolinium? How can we tell? *Magn. Reson. Imaging* **2016**, *34*, 1377–1382. [[CrossRef](#)] [[PubMed](#)]
95. Frenzel, T.; Apte, C.; Jost, G.; Schöckel, L.; Lohrke, J.; Pietsch, H. Quantification and assessment of the chemical form of residual gadolinium in the brain after repeated administration of gadolinium-based contrast agents: Comparative study in rats. *Investig. Radiol.* **2017**, *52*, 396–404. [[CrossRef](#)]
96. Kanal, E. Gadolinium based contrast agents (GBCA): Safety overview after 3 decades of clinical experience. *Magn. Reson. Imaging* **2016**, *34*, 1341–1345. [[CrossRef](#)]
97. Jin, Y.; Chen, S.; Duan, J.; Jia, G.; Zhang, J. Europium-doped Gd₂O₃ nanotubes cause the necrosis of primary mouse bone marrow stromal cells through lysosome and mitochondrion damage. *J. Inorg. Biochem.* **2015**, *146*, 28–36. [[CrossRef](#)]
98. Yang, Y.; Sun, Y.; Liu, Y.; Peng, J.; Wu, Y.; Zhang, Y.; Feng, W.; Li, F. Long-term in vivo biodistribution and toxicity of Gd(OH)₃ nanorods. *Biomaterials* **2013**, *34*, 508–515. [[CrossRef](#)]
99. Grobner, T.; Prischl, F. Gadolinium and nephrogenic systemic fibrosis. *Kidney Int.* **2007**, *72*, 260–264. [[CrossRef](#)] [[PubMed](#)]
100. Penfield, J.G.; Reilly, R.F. What nephrologists need to know about gadolinium. *Nat. Clin. Pr. Nephrol.* **2007**, *3*, 654–668. [[CrossRef](#)] [[PubMed](#)]
101. Boyd, A.S.; Zic, J.A.; Abraham, J.L. Gadolinium deposition in nephrogenic fibrosing dermopathy. *J. Am. Acad. Dermatol.* **2007**, *56*, 27–30. [[CrossRef](#)]
102. High, W.A.; Ayers, R.A.; Chandler, J.; Zito, G.; Cowper, S.E. Gadolinium is detectable within the tissue of patients with nephrogenic systemic fibrosis. *J. Am. Acad. Dermatol.* **2007**, *56*, 21–26. [[CrossRef](#)]
103. Ding, L.; Stilwell, J.; Zhang, T.; Elboudwarej, O.; Jiang, H.; Selegue, J.P.; Cooke, P.A.; Gray, J.W.; Chen, F.F. Molecular Characterization of the Cytotoxic Mechanism of Multiwall Carbon Nanotubes and Nano-Onions on Human Skin Fibroblast. *Nano Lett.* **2005**, *5*, 2448–2464. [[CrossRef](#)] [[PubMed](#)]